The Effect of Asymmetry on the Absolute Instability of Confined Jets and Wakes

Ryan Poole & M. R. Turner

School of Mathematics and Physics, University of Surrey, Guildford. GU2 7XH, UK

Abstract

Jets and wakes are fundamental fluid flows that arise in a wide range of environmental and aerospace applications. They are typically studied as open systems. Here we are interested in the implications of placing the jet or wake inside of another system, as well as the implications of compliant walls. In particular, the effect of asymmetry is considered on the absolute instability properties for this internal flow, when it is transversely confined by compliant walls. Two distinct cases are considered, namely the case of two compliant walls with non-identical wall parameters and the case of identical compliant walls asymmetrically located about the fluid centre line. The absolute instability characteristics are identified by following special saddle points (pinch points) of the dispersion relation in the complex wavenumber plane, and the flow's stability properties are mapped out using parameter continuation techniques. The compliant walls introduce new modes which typically dominate the stability properties of the flow, in comparison to the case of pure shear layers. In the case of symmetrically located walls with non-identical wall parameters, it was found that the absolute stability properties are dominated by the modes linked to the more flexible of the two walls. In the case of identical walls asymmetrically confining the flow, it was found that these flows exhibit smaller regions of absolute instability in parameter space, when compared to the symmetric flow configuration.

1 Introduction

The stability properties of two-dimensional shear flows, such as jets and wakes, is a topic which has achieved significant interest. Jets and wakes typically consist of a central fluid which is sandwiched between two identical outer fluids. All the fluids extend infinitely in the streamwise direction and can be bounded on either side by two walls, as in figure 1, or the outer flows can be unbounded in the transverse direction. In the schematic diagram in figure 1, $U_1 > U_2$ corresponds to a jet, while $U_2 > U_1$ corresponds to a wake. Examining the absolute instability (AI) properties of these jet/wake flows is significant because it has been shown that the existence of an AI in these flows can lead to absolutely unstable global modes downstream, which ultimately cause vortex shedding and hence mixing and turbulence (Huerre and Monkewitz, 1990). Being able to identify global modes is significant as it might be possible to construct a mechanical approach which modifies and controls such absolutely unstable modes, ultimately leading to less downstream turbulence. This could be important when considering sea craft for example, as turbulent wakes from these vessels have been known to impact oceanic ecosystems (Weilgart, 2018).

Confined jets and wakes, similar to that in figure 1, which are symmetric about the flow centreline $z = 0$, have been used as a model for coaxial injectors by Juniper and Candel (2003) and it was shown that the confining walls act as a mechanism to enhance the AI, due to the constructive interference between modes (Juniper, 2007). Poole and Turner (2023) showed that when the rigid planar walls are replaced by identical compliant surfaces, then new instabilities

due to the flexible nature of the walls usually dominate the AI properties and can extend the region of AI for moderate and large confinement parameters. Confinement has also been shown to enhance the AI in other flows, such as the rotating disk boundary layer flow (Healey, 2006), the swirling axisymmetric jet (Healey, 2007) and mixing layers (Healey, 2009).

In the current paper, we consider how the AI properties of the jet/wake flow are affected when the centreline symmetry is broken. In particular we consider two main mechanisms for inducing asymmetry in this flow. Firstly we consider asymmetric confinement, i.e. bounding walls which are placed at different distances from the $z = 0$ line, and secondly we consider the case of non-identical confining walls, i.e. where the walls have different wall parameters.

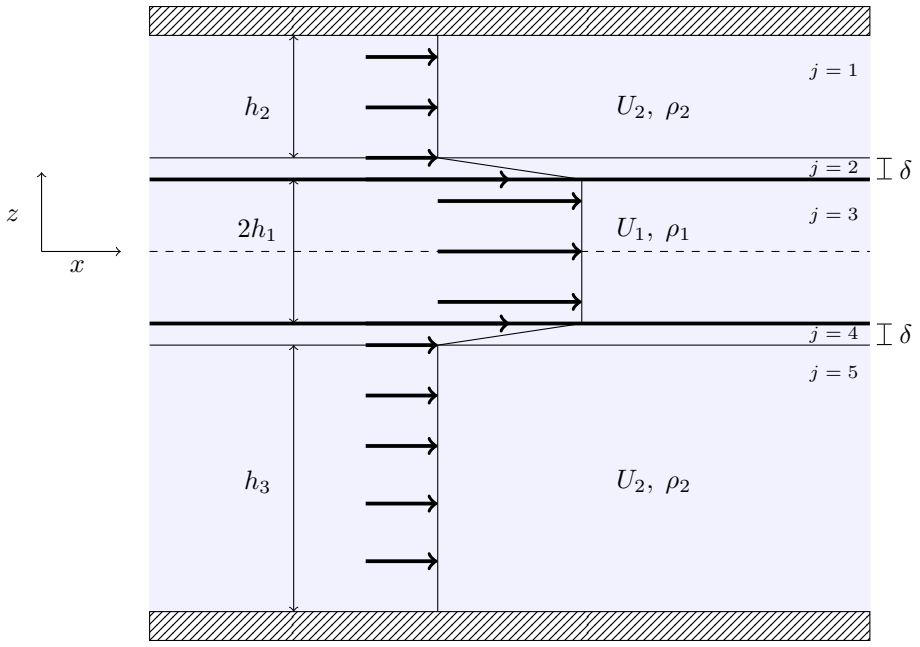

Figure 1: Schematic of the asymmetric plug flow with symmetric shear layers that will be considered in this manuscript. Fluid interfaces are represented by thick black lines at $z = h_1$ and $z = -h_1$ respectively.

The effects of asymmetry on the stability of similar parallel flows to the jet/wake setup have received previous attention. The effects of asymmetric confinement on homogeneous mixing layers has been studied by Healey (2009), who in particular focused on long waves, i.e. $\alpha \ll 1$, where α is the instability wavenumber. In this asymptotic analysis it was shown that the leading order effects of asymmetry were not affected by the smooth nature of the base flow, suggesting that a piecewise linear base flow is sufficient in capturing the main qualitative differences in the system's AI characteristics. Healey (2009) went on to show that asymmetry has a strong stabilizing effect on the flow's temporal instability, but can be destabilizing when we consider the flow's AI characteristics. When compared to the symmetrically confined mixing layer, the asymmetric confined flow was able to induce AI in a region of co-flow, $|\Lambda = \frac{U_1 - U_2}{U_1 + U_2}| < 1$ for a small set of asymmetric confinement values, suggesting that asymmetric confinement can extend the region of AI to lower values of shear. It was also found that for a semi-confined mixing layer (where the flow is only confined on one side by a rigid wall), it is possible to destabilize the flow by placing the confining wall in the faster of the two shear layers, and stabilize it when the confining wall sits in the slower of the two streams. It was noted that when the confining wall is placed in the faster flow that an AI appears at a much lower value of shear for this semi-confined case, $\Lambda \approx 1.15$, when compared to the $\Lambda = 1.32$ seen in the symmetric case. This highlights the possibility that semi-confinement can more readily induce an AI in the flow at lower values of shear. The results for the mixing layer can be compared to our jet/wake flows, since our flow configuration is effectively the combination of two interacting mixing layers, but also because the

asymmetrically confined mixing layer in Healey (2009) is equivalent (i.e. has the same dispersion relation) to the symmetrically confined varicose jet/wake analysis of Juniper (2006).

In the existing literature two other prominent cases of broken symmetry on the stability of parallel flows have been considered. A study carried out by Wang et al. (2019) considers a wake with a piecewise linear base flow with non-identical shear layers of finite thickness, δ_1 and δ_2, at the two fluid interfaces. An asymmetry parameter was defined to be $s = \frac{\delta_1}{\delta_2}$, where $s = 1$ defines the symmetric case. It was shown that increasing the difference between δ_1 and δ_2 leads to a greater difference between the maximum temporal instability growth rates of the varicose modes, which are modes where the waves generated at the fluid interfaces are symmetric about the centre line of the flow and sinuous modes which are interfacial waves which are asymmetric about the centre line of the flow. It was then shown that if one of these shear layers was much thinner than the other, then we can expect the dominant instability at the thin shear layer interface to dominate the temporal instability characteristics of the flow.

It was shown in figure 3(a) of Wang et al. (2019) that there exists three distinct regions of the (δ_1, δ_2) parameter space where three different absolute and convective instability behaviours can be observed. The smallest regions, regions I ($\delta_2 < \delta_1 < 1$) and III ($1 < \delta_2 < \delta_1$), show that if you increase either of δ_1 or δ_2 with the other held fixed, then destabilization and stabilization of the flow are observed respectively. Region II on the other hand, where $\delta_2 < 1 < \delta_1$, highlights a region where, the closer the flow becomes to being symmetric, the more absolutely unstable it becomes. This suggests that the symmetric flow scenario is the most absolutely unstable configuration for the flow. Understanding the properties of a mechanical system such as this is helpful for reducing the drag off wind turbines, where the shear layer off one side of the blade can be considerably larger then that off the other.

A further study carried out by Emerson et al. (2016) examined the effect of an asymmetric density and/or velocity profile, i.e. when the outer two fluids have different densities, or different fluid velocities, on the AI characteristics of a planar wake flow. The asymmetry parameters of the density and velocity profiles were labelled χ_ρ and χ_u respectively. When these parameters are both equal to zero, we have a symmetric wake flow. It was found that increasing the asymmetry of the system, in general, led to the distortion of the varicose and sinuous modes seen in the system, this effect was also seen in the eigenmode plots of Wang et al. (2019). It was shown that increasing χ_ρ led to a destabilizing effect of the flow, while increasing χ_u had a stabilizing effect. This stabilization effect is clear logically since larger χ_u leads to a flow that less resembles a wake, and is more like a simple shear layer, which, for the parameters considered, is in a region of convective instability (CI). These wake profiles with varying density can be useful to study when considering vertically stratified flows, such as in the ocean or the atmosphere for example, where each layer is a different density and each layer may be moving at a different velocity.

The structure of this paper is as follows: in Section 2 we derive the dispersion relations for the two cases noted above, namely asymmetric confinement by identical walls, and symmetric confinement by non-identical walls. Section 3 will discuss the numerical methods used to identify and follow the AI modes as we vary system parameters. In Section 4 we consider how varying the asymmetric characteristics of the flow alters regions of absolute instability (AI) in parameter space. We will primarily consider the limit as the shear layer thickness $\delta \to 0$. We will consider a selection of parameter cases, first for the symmetric confinement of two non-identical planar compliant walls, then for asymmetric confinement by identical compliant walls, and finally for asymmetric confinement by planar rigid walls. Discussions and conclusions can be found in Section 5.

2 Flow Setup and Governing Equations

We consider the two-dimensional flow schematic diagram as shown in figure 1, consisting of five inviscid fluid regions bounded above and below by compliant surfaces. We consider a homogeneous fluid setup with each fluid region having density ρ. The outer two fluids are able to have different thicknesses, h_2 and h_3 for the upper and lower flow respectively, and have constant horizontal velocity $U_2\underline{\widehat{\mathbf{x}}}$, while the inner flow has thickness $2h_1$ and constant horizontal velocity $U_1\underline{\widehat{\mathbf{x}}}$. Here (x, z) are Cartesian coordinates with corresponding unit vectors $\underline{\widehat{\mathbf{x}}}$ and $\underline{\widehat{\mathbf{z}}}$ respectively. While we assume both fluids are inviscid for the purpose of calculating the stability of the flow, we consider the velocities of the two fluids to be continuous through linear shear layers of constant, and equal, thickness δ in the outer fluid. The flow is bounded above and below by two compliant surfaces, where each surface is assumed to have different properties. We model the compliant surfaces as spring backed elastic plates as shown in figure 2. We make the assumption at the outset that these bounding surfaces are only permitted to move in the z-direction, so that the upper surface is located at $z_{\mathrm{s}}^{+} = h_1 + h_2 + \delta + \xi^{+}(x, t)$, and the lower surface is located at $z_{\mathrm{s}}^{-} = -\big(h_1 + h_3 + \delta + \xi^{-}(x, t)\big)$, where $\xi^{\pm}(x, t)$ are the normal displacements from the surfaces' equilibrium positions.

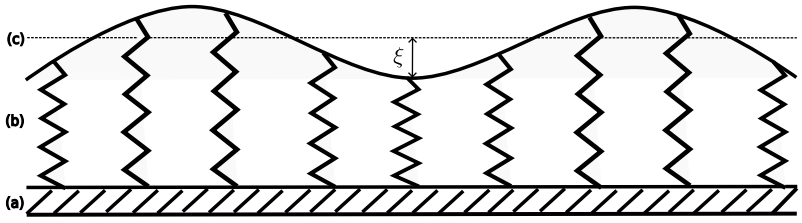

Figure 2: A diagram of the spring-backed elastic plate compliant surface model considered here. The wall is constructed in three layers: (a) the rigid back-plate, (b) a series of identical springs, and (c) a flexible, impermeable membrane. The dotted line represents the wall's unperturbed position, and the distance between this line and the wall is denoted by $\xi(x, t)$.

We consider the base flow to be uni-directional of the form $\mathbf{u} = U(z)\widehat{\mathbf{x}}$ with $U(z)$ given by the piecewise linear flow

$$U(z) = \begin{cases} U^{(1)} = U_2, & h_1 + \delta \leq z \leq z_{\mathrm{s}}^{+} \\ U^{(2)} = (U_2 - U_1)\frac{(z-h_1)}{\delta} + U_1, & h_1 \leq z \leq h_1 + \delta \\ U^{(3)} = U_1, & -h_1 \leq z \leq h_1 \\ U^{(4)} = (U_1 - U_2)\frac{(z+h_1)}{\delta} + U_1, & -h_1 \leq z \leq -(h_1 + \delta) \\ U^{(5)} = U_2, & -(h_1 + \delta) \leq z \leq z_{\mathrm{s}}^{-} \end{cases} \tag{1}$$

where $U^{(j)}$ is the velocity profile in region $j = 1, ..., 5$. It has been shown in Poole and Turner (2023) that the qualitative stability properties of flows of the form (1) are unaffected by the piecewise linear form of the shear velocity profile at leading order when compared to smooth profiles. Hence, we use a piecewise linear profile here in order to obtain qualitative information about the stability properties of this flow. This approach is advantageous because we are able to construct analytical dispersion relations for the instability waves, which can be solved more readily.

In our model we have neglected viscous effects, which most significantly means we have neglected the formation of boundary layers at the walls. In the truly inviscid limit this is a valid assumption but we briefly consider the ramifications of our results when a small, but non-zero,

viscosity is considered. Rienstra and Darau (2011) considered a simple piecewise linear profile analysis which showed that the finite thickness boundary layer has a stabilizing effect on the AI properties of the flow, with the zero thickness boundary layer configuration being the most absolutely unstable. As the boundary layer thickness was increased the AI stabilized completely and the flow became convectively unstable. A similar stabilizing effect was observed in the global AI analysis of Juniper et al. (2011), and Tammisola et al. (2011). The conclusions of Tammisola et al. (2011) found that when the confining walls are sufficiently close to the shear layer, (i.e. when the symmetric confinement parameter is $h = h_2/h_1 \lesssim 1.5$), then the boundary layers work together with the shear layers to stabilize the flow. Strong confinement also has the added effect of reducing the length of the recirculation zone in wake flows, decreasing the instability in the flow further (Juniper et al., 2011). The implication for the results we present in this paper is that at moderate Reynolds numbers our results for $h \lesssim 1.5$ would likely be affected by the resulting shear layers, but for large Reynolds numbers and moderate and weak confinements ($h \gtrsim 1.5$), we expect our results to be relevant.

In each region of our flow we consider the two-dimensional velocity vector $\mathbf{u}^{(j)}(x,z,t) = (u^{(j)}(x,z,t), w^{(j)}(x,z,t))$ for $j = 1, ..., 5$, where the layers are numbered from top to bottom (see figure 1), which satisfy the incompressible Euler equations

$$\frac{\partial \mathbf{u}^{(j)}}{\partial t} + \mathbf{u}^{(j)} \cdot \nabla \mathbf{u}^{(j)} = -\frac{1}{\rho}\nabla p^{(j)}, \tag{2}$$

$$\nabla \cdot \mathbf{u}^{(j)} = 0, \tag{3}$$

where $p^{(j)}(x,z,t)$ is the pressure and ∇ is the two-dimensional gradient operator. In (2), we have neglected gravitational effects as we assume the flow velocities are large and hence gravity is not the main driver for the instabilities (i.e. the Froude number will be large). At $z = z_s^{\pm}$ the flow has to satisfy the governing compliant surface boundary condition, which states that the normal pressure force of the fluid must balance the normal acceleration at the surface, namely

$$p^{(1,5)}(x, z_s^{\pm}, t) = \pm \widehat{\mathbf{n}} \cdot \mathbf{a}, \tag{4}$$

where $\widehat{\mathbf{n}}$ is the unit normal to the wall and $\mathbf{a}$ is the acceleration. In §2.1 we are ultimately interested in linear perturbations of the surface, therefore we only require the component of $\mathbf{a}$ in the $\widehat{\mathbf{z}}$ direction, which we model as a spring backed elastic plate, for which a schematic is given in figure 2, with component

$$\mathbf{a} \cdot \widehat{\mathbf{z}} = \left(m^{\pm}\frac{\partial^2}{\partial t^2} + d^{\pm}\frac{\partial}{\partial t} + B^{\pm}\frac{\partial^4}{\partial x^4} - T^{\pm}\frac{\partial^2}{\partial x^2} + K_E^{\pm} \right) \xi^{\pm}(x,t).$$

The parameters of the compliant surface are, $m^{\pm} = \rho_e^{\pm} b^{\pm}$ the mass per unit area, where $\rho_e^{\pm}$ is the density of the elastic plate, and $b^{\pm}$ is the plate thickness, $d^{\pm}$ the damping coefficient, $B^{\pm}$ the flexural rigidity, which describes the force couple required to bend the plate, while the longitudinal tension of the plate, $T^{\pm}$, measures the tension per unit length. The parameter $K_E^{\pm} = K^{\pm} - g(\rho - \rho_s^{\pm})$ is the 'adjusted' spring stiffness, where $\rho_s^{\pm}$ is the density of the wall substrate and $K^{\pm}$ is the spring stiffness. Note that in the rest of this work, we will redefine $K_E^{\pm}$ as $K^{\pm}$ for simplicity.

At each surface, the fluid must also satisfy the kinematic boundary condition, which due to the assumption of wall motion only in the z-direction, takes the form

$$\frac{\partial \xi^+}{\partial t} + u^{(1)}\frac{\partial \xi^+}{\partial x} = w^{(1)}, \quad \text{and} \quad \frac{\partial \xi^-}{\partial t} + u^{(5)}\frac{\partial \xi^-}{\partial x} = w^{(5)}, \tag{5}$$

at $z = z_s^{\pm}$ respectively.

2.1 Linearization of Problem

To study the stability properties of this flow, we consider small velocities and surface displacements with wavelike properties including a time periodic frequency ω and spatial wavenumber α. Namely, we write

$$\begin{aligned}\mathbf{u}^{(j)}(x,z,t) &= U^{(j)}(z)\widehat{\mathbf{x}} + \epsilon(\widehat{u}^{(j)}(z),\widehat{w}^{(j)}(z))\exp(\mathrm{i}(\alpha x-\omega t)) + \text{c.c},\\ p(x,z,t) &= P^{(j)} + \epsilon\widehat{p}^{(j)}(z)\exp(\mathrm{i}(\alpha x-\omega t)) + \text{c.c},\\ \xi^{\pm}(x,t) &= \epsilon\widehat{\xi}^{\pm}\exp(\mathrm{i}(\alpha x-\omega t)) + \text{c.c},\end{aligned} \tag{6}$$

where $0<\epsilon\ll 1$ is small such that we can linearize (2)-(5), and c.c denotes the complex conjugate. Here $P^{(j)}$ are constant pressures in each layer required to satisfy (2) at $O(1)$ and $\widehat{\xi}^{\pm}$ are constants.

By substituting (6) into (2) and (3), we find that the linear equations at order $O(\epsilon)$ for the flow perturbation quantities are

$$-\mathrm{i}\omega\widehat{u}^{(j)} + \mathrm{i}\alpha U^{(j)}\widehat{u}^{(j)} + \widehat{w}^{(j)}DU^{(j)} = -\frac{\mathrm{i}\alpha}{\rho}\widehat{p}^{(j)}, \tag{7}$$

$$-\mathrm{i}\omega\widehat{w}^{(j)} + \mathrm{i}U^{(j)}\alpha\widehat{w}^{(j)} = -\frac{1}{\rho}D\widehat{p}^{(j)}, \tag{8}$$

$$\mathrm{i}\alpha\widehat{u}^{(j)} + D\widehat{w}^{(j)} = 0, \tag{9}$$

where $D\equiv \mathrm{d}/\mathrm{d}z$. Similarly, we linearize (5) about small normal perturbations by substituting in (6), and to order $O(\epsilon)$ these become

$$-\mathrm{i}\omega\widehat{\xi}^{+} + U_2\mathrm{i}\alpha\widehat{\xi}^{+} = \widehat{w}^{(1)}, \quad \text{and} \quad -\mathrm{i}\omega\widehat{\xi}^{-} + U_2\mathrm{i}\alpha\widehat{\xi}^{-} = \widehat{w}^{(5)}, \tag{10}$$

now evaluated at the equilibrium positions $z=h_1+h_2+\delta$ and $z=-(h_1+h_3+\delta)$ respectively, while linearizing (4) in the same way leads to

$$(-m^{+}\omega^2 - \mathrm{i}\omega d^{+} + B^{+}\alpha^4 + T^{+}\alpha^2 + K^{+})\widehat{\xi}^{+} = \widehat{p}^{(1)}, \quad \text{at} \quad z=h_1+h_2+\delta, \tag{11}$$

$$(-m^{-}\omega^2 - \mathrm{i}\omega d^{-} + B^{-}\alpha^4 + T^{-}\alpha^2 + K^{-})\widehat{\xi}^{-} = -\widehat{p}^{(5)}, \quad \text{at} \quad z=-(h_1+h_3+\delta). \tag{12}$$

2.2 Dispersion Relation

Given the linearized equations (7)-(12), we can now derive the dispersion relation for this flow. First, we eliminate $\widehat{p}^{(j)}$ and $\widehat{u}^{(j)}$ from (7) using (8) and (9) respectively, leading to the Rayleigh equation for the normal velocity perturbation $\widehat{w}^{(j)}$

$$(\alpha U^{(j)}-\omega)(D^2-\alpha^2)\widehat{w}^{(j)} - \alpha D^2U^{(j)}\widehat{w}^{(j)} = 0. \tag{13}$$

In Poole and Turner (2023) the flow scenario was symmetric about $z=0$ and so simplifications could be made by considering only half the flow domain. In the current problem we do not have such symmetry, and so we have to consider both the upper and lower halves of the flow together. Since our base flow (1) is piecewise linear, then $D^2U^{(j)}=0$ in each layer, thus (13) reduces to $(D^2-\alpha^2)\widehat{w}^{(j)}=0$, with solutions in each layer written as

$$\widehat{w}^{(1)} = A_1\exp(\alpha(z-(h_1+\delta))) + B_1\exp(-\alpha(z-(h_1+\delta))), \tag{14}$$

$$\widehat{w}^{(2)} = A_2\cosh(\alpha(z-h_1)) + B_2\sinh(\alpha(z-h_1)), \tag{15}$$

$$\widehat{w}^{(3)} = A_3\cosh(\alpha z) + B_3\sinh(\alpha z), \tag{16}$$

$$\widehat{w}^{(4)} = A_4\cosh(\alpha(z+h_1)) + B_4\sinh(\alpha(z+h_1)), \tag{17}$$

$$\widehat{w}^{(5)} = A_5\exp(\alpha(z+(h_1+\delta))) + B_5\exp(-\alpha(z+(h_1+\delta))). \tag{18}$$

We use the explicit exponential function form in layers 1 and 5 so that comparison with the works of Juniper (2007) and Poole and Turner (2023) can be readily made.

At the interfaces of the different base profile regions, namely at $z = \pm h_1$ and $z = \pm(h_1 + \delta)$, we require that both the displacement of the fluid interface and the perturbation pressure are continuous, which leads to the jump conditions

$$\Delta\left[\frac{\widehat{w}^{(j)}}{\alpha U^{(j)} - \omega}\right] = 0, \quad \text{and} \quad \Delta\left[\rho(\alpha U^{(j)} - \omega)D\widehat{w}^{(j)} - \alpha\rho DU^{(j)}\widehat{w}^{(j)}\right] = 0, \tag{19}$$

respectively, where $\Delta[\cdot] = \lim_{\zeta\to 0}[\cdot]_{z_n-\zeta}^{z_n+\zeta}$ and z_n is the equilibrium interface position (Drazin, 2002). Now we require a usable form for our boundary conditions at the upper and lower compliant surfaces. Using (10) together with (7)-(9), we can write the boundary conditions (11)-(12) as

$$\begin{aligned} Q^{+}\widehat{w}^{(1)} &= \frac{\rho}{\alpha^2}(\alpha U_2 - \omega)^2 D\widehat{w}^{(1)}, \\ Q^{-}\widehat{w}^{(5)} &= -\frac{\rho}{\alpha^2}(\alpha U_2 - \omega)^2 D\widehat{w}^{(5)}, \end{aligned} \tag{20}$$

at $z = h_1 + h_2 + \delta$ and $z = -(h_1 + h_3 + \delta)$ respectively. We define $Q^{\pm}(\alpha, \omega) = (-m^{\pm}\omega^2 - \mathrm{i}\omega d^{\pm} + B^{\pm}\alpha^4 + T^{\pm}\alpha^2 + K^{\pm})$ to be the wall compliance at the upper and lower surfaces, and this quantity is related to the wall impedance term used to model acoustic wall linings (Brambley, 2009). Substituting in the expressions for $\widehat{w}^{(1)}$ and $\widehat{w}^{(5)}$ from (14) and (18), we can write these conditions in the compact forms

$$\frac{A_1}{B_1} = -e^{-2\alpha h_2}\left[\frac{Q^{+} + \rho(\alpha U_2 - \omega)^2}{Q^{+} - \rho(\alpha U_2 - \omega)^2}\right], \tag{21}$$

$$\frac{B_5}{A_5} = -e^{-2\alpha h_3}\left[\frac{Q^{-} + \rho(\alpha U_2 - \omega)^2}{Q^{-} - \rho(\alpha U_2 - \omega)^2}\right], \tag{22}$$

where in the limit as $Q^{\pm} \to \infty$, the compliant surfaces become rigid walls and we obtain the boundary condition for a rigid wall bounded flow (Juniper, 2007). For more details on how to derive dispersion relations for piecewise linear flow profiles the reader is referred to Drazin and Reid (2004); Drazin (2002).

By considering the jump conditions (19) at each regional interface, together with the boundary conditions (21) and (22), we arrive at a system of 10 equations for the 11 unknowns A_{1-5}, B_{1-5} and ω (assuming α is given). Hence eliminating A_{1-5} and B_{1-5} leads to a dispersion relation ($\mathbb{D}(\alpha, \omega) = 0$) for unknown $\omega(\alpha)$. At this stage we also non-dimensionalise the system. Hence by taking h_1 as our characteristic length scale, $U_{\mathrm{ref}} = (U_1 + U_2)/2$ as our characteristic velocity scale, letting the shear layer thickness $\delta = \delta^* h_1$ and defining the confinement ratios $h = h_2/h_1$, $\widetilde{h} = h_3/h_1$, along with the non-dimensional parameters

$$\begin{aligned} m^{\pm} &= \rho h_1 m^{\pm *}, & d^{\pm} &= \rho U_{\mathrm{ref}} d^{\pm *}, & B^{\pm} &= \rho h_1^3 U_{\mathrm{ref}}^2 B^{\pm *}, \\ T^{\pm} &= \rho h_1 U_{\mathrm{ref}}^2 T^{\pm *}, & K^{\pm} &= \frac{\rho U_{\mathrm{ref}}^2}{h_1} K^{\pm *}, & Q^{\pm} &= \frac{\rho U_{\mathrm{ref}}^2}{h_1} Q^{\pm *}, \\ \alpha &= \alpha^*/h_1, & \omega &= \omega^* U_{\mathrm{ref}}/h_1, & \Lambda &= \frac{U_1 - U_2}{U_1 + U_2}, \end{aligned} \tag{23}$$

we derive the dispersion relation

$$\mathbb{D}(\alpha^*,\omega^*) \equiv \left[\alpha^* Q^{+*}(-e^{-2\alpha^* h}D_+^{v*} + D_-^{v*}) + (\alpha^*(1-\Lambda)-\omega^*)^2(-e^{-2\alpha^* h}D_+^{v*} - D_-^{v*})\right]\times \\ \left[\alpha^* Q^{-*}(-e^{-2\alpha^* \widetilde{h}}D_+^{s*} + D_-^{s*}) + (\alpha^*(1-\Lambda)-\omega^*)^2(-e^{-2\alpha^* \widetilde{h}}D_+^{s*} - D_-^{s*})\right] + \\ \left[\alpha^* Q^{-*}(-e^{-2\alpha^* \widetilde{h}}D_+^{v*} + D_-^{v*}) + (\alpha^*(1-\Lambda)-\omega^*)^2(-e^{-2\alpha^* \widetilde{h}}D_+^{v*} - D_-^{v*})\right]\times \\ \left[\alpha^* Q^{+*}(-e^{-2\alpha^* h}D_+^{s*} + D_-^{s*}) + (\alpha^*(1-\Lambda)-\omega^*)^2(-e^{-2\alpha^* h}D_+^{s*} - D_-^{s*})\right] = 0. \quad (24)$$

The non-dimensional quantity Λ is a measure of the shear between the inner and outer fluid flows. When $\Lambda > 0$ we have a jet, and when $\Lambda < 0$ we have a wake.

In (24) $*$ denotes a dimensionless quantity and

$$D_\pm^{v*} \equiv [\delta^*(\omega^* - \alpha^*(1+\Lambda))\coth(\alpha^*) + 2\Lambda]\,[\delta^*(\omega^* - \alpha^*(1-\Lambda))(\cosh(\alpha^*\delta^*) \mp \sinh(\alpha^*\delta^*)) \\ -2\Lambda\sinh(\alpha^*\delta^*)] \mp (\omega^* - \alpha^*(1+\Lambda))\delta^*\,[\delta^*(\omega - \alpha^*(1-\Lambda))(\cosh(\alpha^*\delta^*) \mp \sinh(\alpha^*\delta^*)) \pm 2\Lambda\cosh(\alpha^*\delta^*)], \quad (25)$$

while $D_\pm^{s*}$ has the same structure, except with the $\coth(\alpha^*)$ replaced by $\tanh(\alpha^*)$. In what follows we drop the $*$ notation on the dimensionless quantities with the understanding that now everything is dimensionless. We use the superscripts v and s on the terms in (25), because in Poole and Turner (2023), when the flow was symmetrically confined, the D^v and D^s terms related to components of the dispersion relation for varicose modes (antisymmetric $\widehat{w}$ about $z = 0$) and sinuous modes (symmetric $\widehat{w}$ about $z = 0$) respectively, which in that case could be examined separately. In this asymmetric case these distinctions do not exist, but it is useful to keep this notation as the modes will have properties similar to varicose or sinuous modes from the symmetric limit.

In the case where $h = \widetilde{h}$ with symmetric wall parameters ($Q^- \equiv Q^+ \equiv Q$), (24) reduces to

$$\mathbb{D}(\alpha,\omega) \equiv \left[\alpha Q(-e^{-2\alpha h}D_+^v + D_-^v) + (\alpha(1-\Lambda)-\omega)^2(-e^{-2\alpha h}D_+^v - D_-^v)\right]\times \\ \left[\alpha Q(-e^{-2\alpha h}D_+^s + D_-^s) + (\alpha(1-\Lambda)-\omega)^2(-e^{-2\alpha h}D_+^s - D_-^s)\right] = 0, \quad (26)$$

i.e. here the sinuous and varicose modes decouple as expected. In the limit $\delta \to 0$, (24) simplifies such that at $O(\delta)$

$$\mathbb{D}(\alpha,\omega) \equiv \left[\alpha Q^- X^v(\widetilde{h}) - (\alpha(1-\Lambda)-\omega)^2 Y^v(\widetilde{h})\right]\left[\alpha Q^+ X^s(h) - (\alpha(1-\Lambda)-\omega)^2 Y^s(h)\right] \\ + \left[\alpha Q^- X^s(\widetilde{h}) - (\alpha(1-\Lambda)-\omega)^2 Y^s(\widetilde{h})\right]\left[\alpha Q^+ X^v(h) - (\alpha(1-\Lambda)-\omega)^2 Y^v(h)\right] = 0, \quad (27)$$

where

$$X^v(\zeta) = (\alpha(1-\Lambda)-\omega)^2\coth(\alpha\zeta) + (\alpha(1+\Lambda)-\omega)^2\coth(\alpha), \\ Y^v(\zeta) = (\alpha(1-\Lambda)-\omega)^2 + (\alpha(1+\Lambda)-\omega)^2\coth(\alpha)\coth(\alpha\zeta), \quad (28)$$

and for $X^s(\zeta), Y^s(\zeta)$ we replace the $\coth(\alpha)$ terms with $\tanh(\alpha)$. In this limit, the case $h = \widetilde{h}$ with $Q^+ = Q^- = Q$ in (27) gives the equations studied by Poole and Turner (2023), also $X^{s,v}$ are identical to the rigid wall dispersion relations derived by Juniper (2006) for $h = \widetilde{h}$ and $Q^\pm \to \infty$.

By considering (27), we can consider two different ways in which we can break the centre-line symmetry of the flow:

1. Different confining surfaces ($Q^- \neq Q^+$) but with symmetric confinement ($h = \widetilde{h}$),

2. Identical confining surfaces ($Q^- = Q^+$), including the rigid wall limit, but with asymmetric confinement ($h \neq \widetilde{h}$).

There is of course the third case when $Q^- \neq Q^+$ and the confinement is asymmetric ($h \neq \widetilde{h}$), but this case isn't explicitly examined here as it is just the combination of cases 1 and 2.

Both dispersion relations (24) and (27) are 8^{th} order polynomials in ω with transcendental coefficients in α. In this paper, we study the two above cases independently. Following the study of Poole and Turner (2023), the inclusion of compliant bounding surfaces in jet/wake flows identifies two families of modes present in the system: Shear-induced (SI) modes are modes present in the flow when the surfaces are considered to be rigid planar walls, and are driven by the presence of the shear layers; Wall-induced (WI) modes are modes which are present in the flow due to the inclusion of the compliant walls. How these modes behave and interact with one another is explored in detail for the symmetrically confined problem by Poole and Turner (2023), and the reader is referred here for more details.

3 Identifying Absolute Instabilities

In this article our interest lies in calculating the AI properties of the asymmetric flows detailed in §2, which due to them being parallel flows, will also constitute a global instability. In order to identify an AI we consider the differential equation associated with our dispersion relation $\mathbb{D}(\alpha, \omega) = 0$, which is

$$\mathbb{D}\Big(-\mathrm{i}\frac{\partial}{\partial x}, \mathrm{i}\frac{\partial}{\partial t}\Big) w(x, z, t) = 0. \tag{29}$$

We seek solutions of this differential equation which are initialized by an impulse forcing at the origin. Thus we seek solutions to the impulsive form of (29) such that the right hand side is equal to $\delta(x)\delta(t)\widehat{w}(z)$, where δ is the Dirac delta function. Then if the solution has the property that

$$\lim_{t\to\infty} |w(x, z, t)| \to \infty,$$

along the characteristic $x/t = 0$, then the flow is absolutely unstable (Schmid et al., 2002). This is a Green's function representation of an AI, the solution of which can also be represented as

$$w(x, z, t) = \int_L \int_F \frac{\widehat{w}(z)}{\mathbb{D}(\alpha, \omega)} \exp\left[\mathrm{i}(\alpha x - \omega t)\right] \, \mathrm{d}\alpha \mathrm{d}\omega, \tag{30}$$

after taking the inverse Fourier transform in x and inverse Laplace transform in time t. Here F is the Fourier inversion contour that sits along the real α-axis, while the Laplace inversion contour L sits above all singularities in the complex ω-plane for causality (Schmid et al., 2002). If we have no stability mechanism for the short instability waves of the system, such as surface tension, viscosity or a non-zero shear layer thickness between the flows, then we have an infinite number of singularities in the ω-plane at large $\omega_i = \mathrm{Im}(\omega)$. This leads to an ill posed problem because essentially we cannot place L above all these points. To overcome this we consider the existence of a small, but finite, stabilization mechanism, here we use shear layers, and let this tend to zero.

The response (30) is essentially unaffected by the structure of the response in the z-direction (Juniper, 2007), with the main restriction being that it is isolated in x and t at the shear layers $z = \pm 1$. In this work we do not consider the so called full response (Healey, 2006; Juniper, 2007) to the forcing, which considers the growth of the disturbance in the outer fluid, away from the shear layer.

We solve the first integral of (30) by means of Cauchy's residue theorem, which gives

$$w(x, z, t) = \frac{1}{2\pi} \sum_m \int_F \frac{\widehat{w}(z)}{\mathbb{D}_\omega(\alpha, \omega_m)} \exp\left[\mathrm{i}t\left(\alpha\frac{x}{t} - \omega_m\right)\right] \, \mathrm{d}\alpha, \tag{31}$$

where the sum is over the residues of m singularities in the ω-plane. To approximate the final inverse Fourier transform integral, we consider the large time limit, $t \to \infty$, which by using the method of steepest descent, amounts to calculating the value of ω_i at special saddle points in the complex α-plane. These special saddle points are known as pinch points.

To determine the values of α and ω at these special saddle points we solve the pair of equations

$$\mathbb{D}(\alpha, \omega) = \frac{\partial \mathbb{D}(\alpha, \omega)}{\partial \alpha} = 0, \tag{32}$$

simultaneously using Newton's method, starting with an initial guess (α^0, ω^0), which we obtain by sight from plotting contours of constant ω_i in the complex α-plane. At each step the $(n+1)^{\text{th}}$ iterate is given via

$$\begin{pmatrix} \alpha^{n+1} \\ \omega^{n+1} \end{pmatrix} = \begin{pmatrix} \alpha^{n} \\ \omega^{n} \end{pmatrix} - \begin{pmatrix} \mathbb{D}_\alpha(\alpha^n, \omega^n) & \mathbb{D}_\omega(\alpha^n, \omega^n) \\ \mathbb{D}_{\alpha\alpha}(\alpha^n, \omega^n) & \mathbb{D}_{\alpha\omega}(\alpha^n, \omega^n) \end{pmatrix}^{-1} \begin{pmatrix} \mathbb{D}(\alpha^n, \omega^n) \\ \mathbb{D}_\alpha(\alpha^n, \omega^n) \end{pmatrix}, \tag{33}$$

where the subscripts denote partial derivatives. Iterations are continued until $||(\alpha^{n+1}, \omega^{n+1}) - (\alpha^n, \omega^n)||_2 < 10^{-8}$.

This numerical approach identifies saddle points and the value of ω_i at those points, but to determine whether they are pinch points we use the Briggs criterion (Briggs et al., 1964). This effectively states that the hills that make a saddle point originate from different sides of the inversion contour F. In most cases, this can easily be determined by observation (Healey, 2006), however sometimes the path of F is ambiguous (usually due to the existence of multiple Riemann sheets of the α-plane, as presented in figure 4(a), where the inversion contour is plotted in red.), and in those cases we can resort to numerically integrating along the real α-axis in (31) using the arbitrary precision package of Smith (1991). This technique of numerically verifying whether a saddle point is a pinch points was also carried out in Healey (2006) who evaluated the Fourier inversion integral along a path of decaying eigenfunctions in the wall-normal direction. Using this approach Healey was able to highlight an example of saddle points switching dominance in figure 5 of the same paper. The arbitrary precision is required so that the rapidly varying integrand of (31) can be handled efficiently. In this case the numerically calculated complex frequency is given by

$$\omega^{\text{num}} = \frac{\mathrm{i} w_t(0, 1, t)}{w(0, 1, t)}, \tag{34}$$

where the subscript t denotes the partial derivative. In the limit $t \to \infty$ (34) gives the same value as ω at the dominant pinch point in the α-plane, hence $\mathrm{Im}(\omega^{\text{num}}) = \omega_i^{\text{num}}$ gives the same growth rate as the pinch point, ω_i. For these ambiguous cases, we consider results with finite shear layer thickness $\delta \neq 0$, which acts as a stabilization mechanism for short-waves (large α values)[1], such that the form of (30) is well posed, and the arbitrary precision numerics can be carried out, and then we let $\delta \to 0$ to understand what happens in the $\delta = 0$ case.

In problems such as the one considered here, we must be careful to calculate the growth rate of modes related to all pinch points, and to keep track of their pinch point status, because as we vary the system parameters, and use continuation techniques to follow the saddles, the dominant saddle point can switch between saddles, and their pinch point status can change as they fall on and off the Fourier inversion contour.

[1]We note that varying wall parameters does not have the same short-wave stabilization effect on the temporal instability of SI modes as increasing the shear layer thickness, as shown in Poole and Turner (2023), hence the only mechanism to make (30) well-posed in our problem is increasing the shear layer thickness.

4 Results

4.1 Non-Identical Compliant Walls with Symmetric Confinement

First we consider the effect of non-identical walls when symmetrically confining a jet/wake flow with walls at $z_s^{\pm} = \pm(1+h)$. Using equations (26)-(27) we initially consider how non-identical compliant walls affect the velocity eigenmodes of the flow using real α and complex ω values. We then examine how varying the parameters of the walls influence the flow's AI characteristics. In the results which follow we consider the infinitely thin shear layer case $\delta \to 0$, unless stated otherwise.

4.1.1 Velocity Eigenmodes

Here we consider the effect of non-identical walls on both wall-induced (WI) and shear-induced (SI) modes of instability. We consider the form of the eigenmodes for both vertical and horizontal velocity components of the perturbation, $\widehat{w}(z)$ and $\widehat{u}(z)$ respectively and we consider the most temporally unstable mode for each case. The vertical perturbation velocity eigenmodes in the limit $\delta \to 0$ take the form

$$\widehat{w}^{(1)} = \exp(-\alpha(z-1)) - \Pi^{+}\exp(\alpha(z-(1+2h))), \tag{35}$$

$$\widehat{w}^{(3)} = A_3\cosh(\alpha h) + B_3\sinh(\alpha h), \tag{36}$$

$$\widehat{w}^{(5)} = A_5\Big[\exp(\alpha(z+1)) - \Pi^{-}\exp(-\alpha(z+1+2h))\Big], \tag{37}$$

where the $\widehat{u}^{(j)}(z)$ functions are calculated via (9) such that

$$\widehat{u}^{(j)}(z) = \frac{\mathrm{i}D\widehat{w}^{(j)}(z)}{\alpha}. \tag{38}$$

The coefficients appearing in these expressions are defined to be

$$A_3 = \frac{Z^2E^{-}\cosh(\alpha) + E^{+}\sinh(\alpha)}{Z},$$
$$B_3 = \frac{ZE^{-} - A_3\cosh(\alpha)}{\sinh(\alpha)},$$
$$A_5 = \frac{Z(B_3\cosh(\alpha) - A_3\sinh(\alpha))}{\widetilde{E}},$$

where $Z = \dfrac{\alpha(1+\Lambda)-\omega}{\alpha(1-\Lambda)-\omega}$, $E^{\pm} = 1 \pm \Pi^{+}\exp(-2\alpha h)$ and $\widetilde{E} = 1 + \Pi^{-}\exp(-2\alpha\widetilde{h})$, where

$$\Pi^{\pm} = \frac{\alpha Q^{\pm} + (\alpha(1-\Lambda)-\omega)^2}{\alpha Q^{\pm} - (\alpha(1-\Lambda)-\omega)^2}.$$

We fix the upper wall to be compliant, with parameters

$$(B^{+}, T^{+}, K^{+}, m^{+}, d^{+}) = (1, 2, 2, 1.2, 0.001), \tag{39}$$

while the lower wall is identical in all parameters except the flexural rigidity B^{-}. We use these parameters, because both the most unstable SI and WI modes are temporally unstable in this case. We consider 3 different values of B^{-}, such that $B^{-} < B^{+}$, $B^{-} = B^{+}$, $B^{-} > B^{+}$, and we also fix the shear parameter $\Lambda = -2$ and the wavenumber $\alpha = 1$. The eigenmodes are plotted in figure 3 and are normalized such that the 2-norm of each mode is equal to 1. We consider the most temporally unstable SI (solid lines) and WI (dash-dot lines) mode at each configuration.

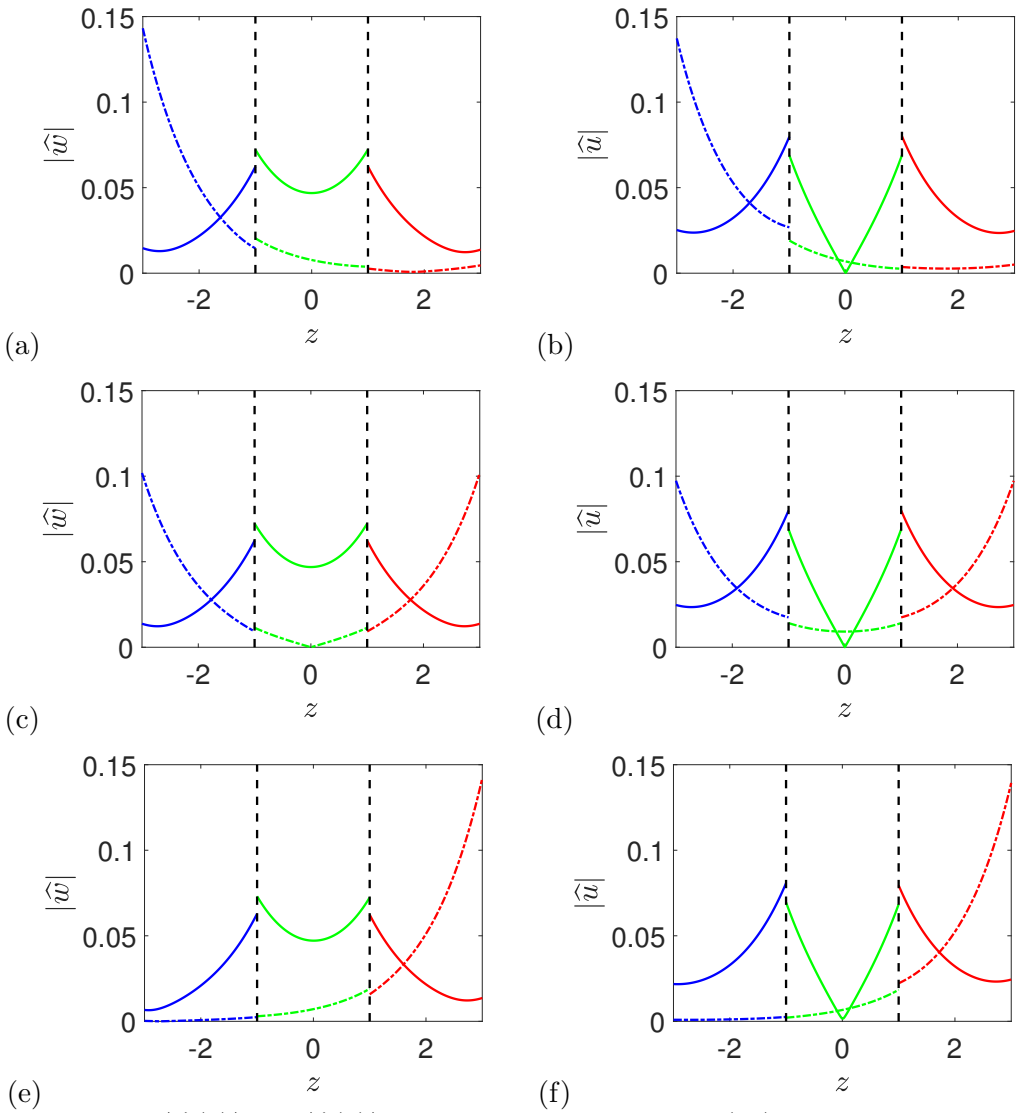

Figure 3: Plots of $|\widehat{w}(z)|$ and $|\widehat{u}(z)|$ at the wall configurations (39), with $\alpha = 1, \Lambda = -2, h = 2$, and (a,b) $B^- = 0.5$, (c,d) $B^- = 1$ and (e,f) $B^- = 10$, with $B^+ = 1$ fixed. Solid lines denote the SI mode while dot-dashed lines denote the WI mode. Black dashed lines at $z = \pm 1$ indicate the fluid interfaces. These eigenmodes have been normalised such that $||\widehat{w}||_2 = ||\widehat{u}||_2 = 1$.

In the symmetric limit, figures 3(c) and (d), we find that the WI mode reaches its maximum velocity at the walls, while the SI modes reach a maximum velocity at the fluid interfaces at $z = \pm 1$ as expected. When we increase the value of B^- at the lower wall at $z = z_s^- = -3$ to $B^- = 10$ in figures 3(e) and (f), we find that the values of $|\widehat{w}|$ and $|\widehat{u}|$ are much smaller at $z = z_s^- = -3$ for the WI modes, whereas the SI modes are relatively unaffected. This makes sense, since as we increase B^- we move closer to the rigid wall limit, i.e. $B^- \to \infty$ for example, where we expect the rigid wall boundary conditions to hold, namely that $\widehat{w} = 0$. The eigenmode shape at the fixed compliant wall at $z = z_s^+ = 3$ is still a maximum, but in fact what is striking is that the difference between the WI mode at the upper wall compared to the lower wall is considerably different.

Making the lower wall more flexible than the fixed wall, with $B^- = 0.5$ in figures 3(a) and (b), we find that the effect is reversed and now the lower wall produces a significantly larger value of $|\widehat{w}|$ than at the upper wall. This shows that the instability perturbation is concentrated at the least rigid of the two walls.

4.1.2 AI Analysis

Now we consider the effect of symmetrically confined non-identical compliant walls on the AI characteristics of the jet/wake flow. We set both wall parameters to be

$$(B^{\pm}, T^{\pm}, K^{\pm}, m^{\pm}, d^{\pm}) = (2, 0, 10, 0.1, 0) \tag{40}$$

for the symmetric configuration and then we consider variations of the lower wall parameters.

First we consider the effect of these non-identical walls on the complex α-plane, presented in figure 4 with $\Lambda = 1, h = 2$, as we vary B^-. We plot contours of constant ω_i in the complex α-plane via the dispersion relation, and modes of instability then take the form of special saddle points, namely pinch points. These correspond to either an AI mode when $\omega_i > 0$ at the saddle point, or a convectively unstable or stable mode otherwise (Juniper, 2006; Poole and Turner, 2023; Schmid et al., 2002).

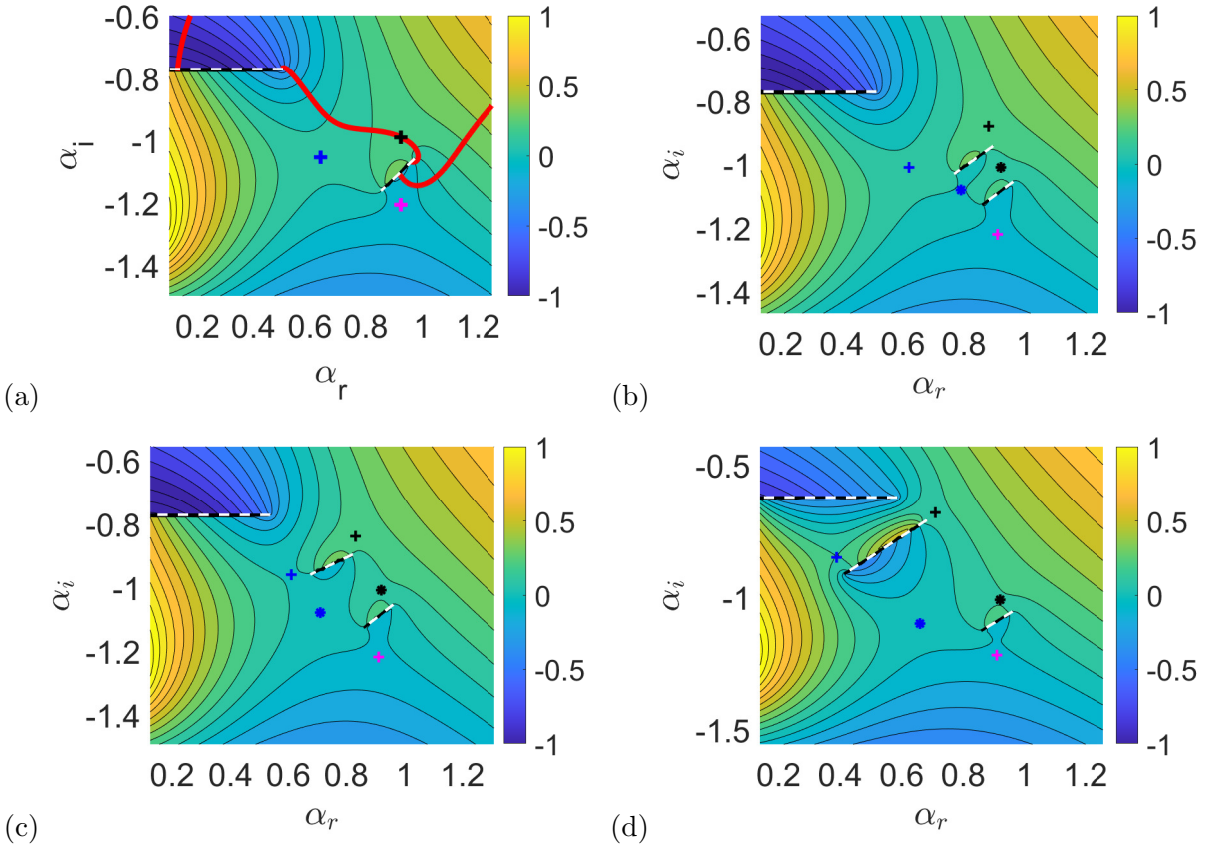

Figure 4: Contours of constant ω_i in the complex α-plane for 4 different wall configurations: (a) symmetric walls with $B^- = B^+ = 2$, (b) $B^- = 3$, (c) $B^- = 4$ and (d) $B^- = 10$. We fix $\Lambda = 1, h = 2$. Blue markers indicate SI modes, while black and magenta markers indicate WI modes. Branch cuts are represented by black and white dashed lines, and the red contour in figure (a) represents a possible inversion contour.

We consider 4 values of the lower wall flexural rigidity B^-; the symmetric configuration has $B^- = B^+$, with modes SI, WI_1 and WI_2 visible in figure 4(a) represented by blue, black and magenta crosses. Here WI_1 and WI_2 indicate that we have two wall-induced modes of interest. The remaining three configurations have $B^- > B^+$, with B^- gradually increasing in each figure. For the symmetric case in figure 4(a) the blue cross is the saddle point which dominates in the rigid wall limit, while Poole and Turner (2023) showed that when the walls are compliant (and identical) additional saddles are generated in the complex α-plane. In this case it was shown that the generated black cross saddle is also a pinch point, and because it lies in the hills of

the SI saddle, it has a larger value of ω_i and hence dominates the AI characteristics of the flow. By increasing B^- away from this symmetric state this has the effect of dividing the smaller branch cut in figure 4(a), where in figure 4(a) the two branch cuts overlap one another. This dividing has the effect of introducing an additional set of modes which become pinch points as B^- continues to increase. These new modes, seen in figures 4(b-d) are denoted with blue and black dots and are referred to as SI$'$ and WI$_1'$ modes. The colour of these markers correlate with the SI and WI$_1$ modes. We note that the blue modes are always subdominant to the black modes for these system parameters.

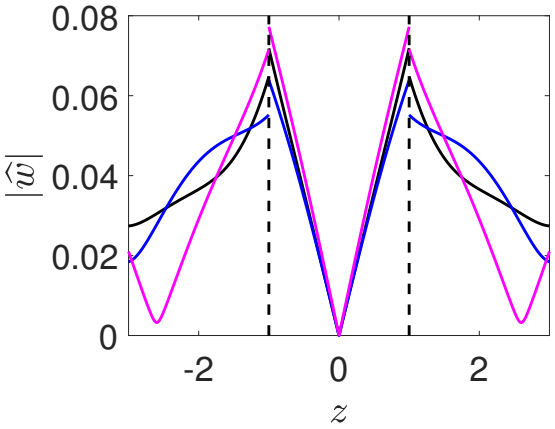

Figure 5: Comparison of $|\widehat{w}|$ eigenmodes for the three AI modes in figure 4(a), where the colour of each mode corresponds to the colour cross used to indicate each mode. Vertical dashed lines indicate fluid interfaces, and these modes have been normalized such that $||\widehat{w}||_2 = 1$.

The branch cuts in figure 4 indicate that Riemann sheets of the WI and SI modes, discussed for the temporal problem, are now connected, and as a result, we expect these modes to have characteristics of both SI and WI modes, as shown in figure 5. These AI modes are those modes in figure 4(a) and have peaks in magnitude at the shear layers and relatively large values at the walls. Thus when we refer to SI modes in this context, we are referring to those modes which persist in the complex plane when the walls are rigid, and WI modes as those modes which are the additionally generated modes when the wall(s) are compliant.

As the difference between B^- and B^+ increases, the positions of modes SI and WI$_1$ change while the positions of the SI$'$, WI$_1'$ and WI$_2$ modes remain relatively fixed. This suggests that these first two modes are strongly connected to the behaviour of the modified lower wall, whose parameters are changing, while the other modes being static suggests their behaviour relates to the upper wall, whose parameters are fixed. Hence in the case $B^- \to \infty$ when the lower wall is rigid, the presence of the compliant upper wall is still able to induce these WI modes in the system. Note, a similar behaviour to the one seen in figure 4 is observed when a different lower wall parameter other than B^- is varied.

By considering the effects of varying B^- on the α-plane, it is clear that non-identical walls contribute additional modes to the instability characteristics of the flow, and may allow an AI to persist even into the semi-rigid wall limit, where one wall is taken to be rigid and the other compliant. To explore the effects of varying the wall parameters, we consider regions of AI in $(\Lambda^{-1}, h)-$space for four non-identical wall configurations, shown in figure 6. These region plots are created using the method outlined in Appendix C of Rees and Juniper (2010) where we essentially follow the neutral ω_i modes in (Λ^{-1}, h)-space. The grey regions indicate regions of AI, where the solid black lines indicate the AI-CI boundaries. The dashed lines and the dot-dashed lines indicate the AI-CI boundaries of the two symmetric configurations, when both walls have identical parameters. In these figures, we specifically focus on the AI-CI boundaries of WI modes as these are the first modes to become absolutely unstable as we increase the shear

value, Λ. What we are interested in here is whether the size of the AI region for asymmetrically confined flows is larger than either of the symmetrically confined flows, and this occurs if the solid line lies beyond both the dashed and dot-dashed lines.

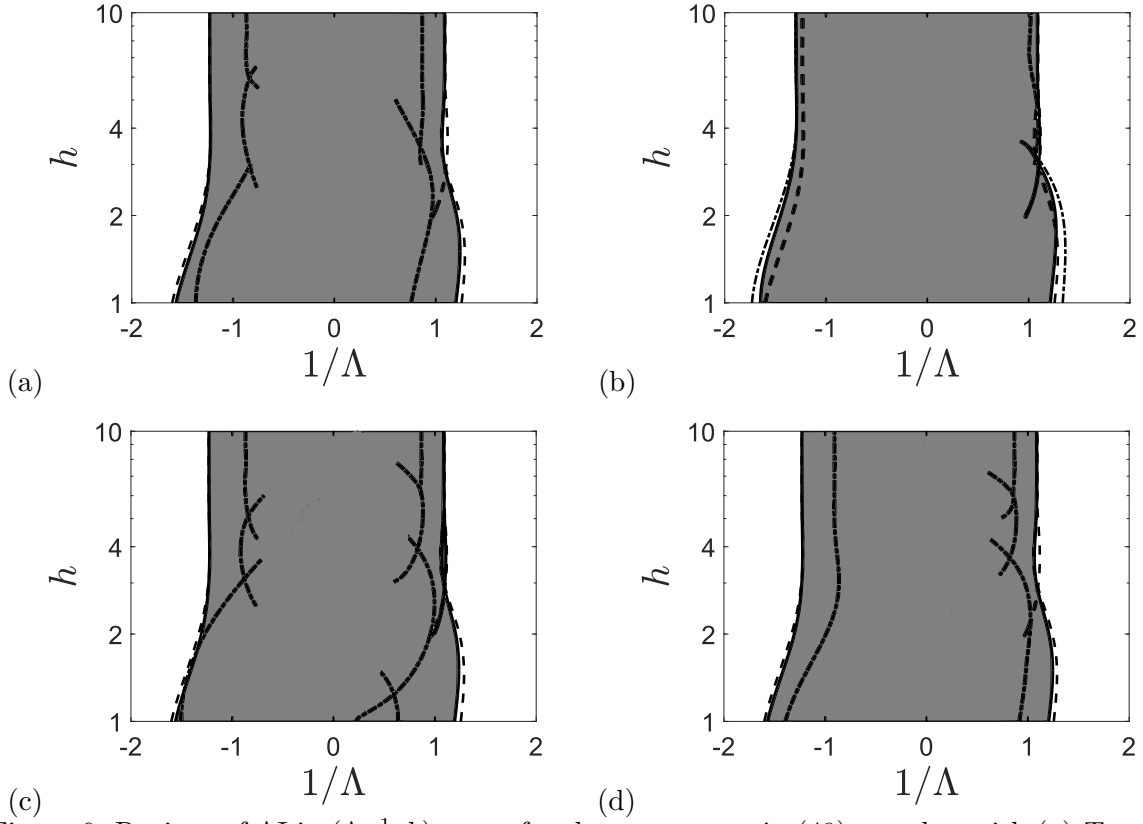

Figure 6: Regions of AI in (Λ^{-1}, h)-space for the parameters in (40) together with (a) $T^- = 10$, (b) $K^- = 5$, (c) $m^- = 25$ and (d) $d^- = 5$ given by the solid lines. The dashed lines represent the regions of AI for the flow with symmetric wall configuration with parameters (40), while the dot-dashed lines give the symmetric wall configuration with (a) $T^{\pm} = 10$, (b) $K^{\pm} = 5$, (c) $m^{\pm} = 25$ and (d) $d^{\pm} = 5$.

We find that when varying any of the wall parameters from the symmetric configuration, in such a way as to make one wall more rigid, we observe a small stabilizing effect at small h, as seen by the shrinking AI regions in figure 6(a), (c) and (d). The effect on the region at weak confinement values is less pronounced. Figure 6(b) on the other hand shows the effect of reducing the spring constant $K^- = 5$, i.e. making one wall more flexible, which has a destabilizing effect for $\Lambda < 0$. This destabilizing behaviour is more prominent when decreasing K^- further. Furthermore, for $\Lambda > 0$, we now see the AI-CI boundaries of two modes, suggesting that we observe a new WI mode appearing in a similar way to that shown in figure 4. However, in all the panels in figure 6, we find that the region for asymmetric confinement is always bounded by the two symmetric configurations, suggesting that for these parameters the symmetric configuration is the most unstable. What these results do show however, is that when the walls have different parameters, the lighter, more flexible wall appears to govern the AI characteristics of the flow.

Since we have shown that varying B^- allows for new modes to appear and become dominant in figure 4, we now focus specifically on varying B^- with the AI-CI regions shown in figure 7. It is clear that as we vary B^- we again see very little variation in the size and shape of the AI regions compared to the two symmetric configurations, similar to figure 6. This is certainly the case when B^- is of similar magnitude to B^+, as in figures 7(a) and (b). As we increase B^- to $B^- = 15$ in figure 7(c) we do see regions in the (Λ^{-1}, h)-plane where we now have AI which were CI in the $B^{\pm} = 2$ symmetric limit (dashed lines). This again can be seen for moderate values

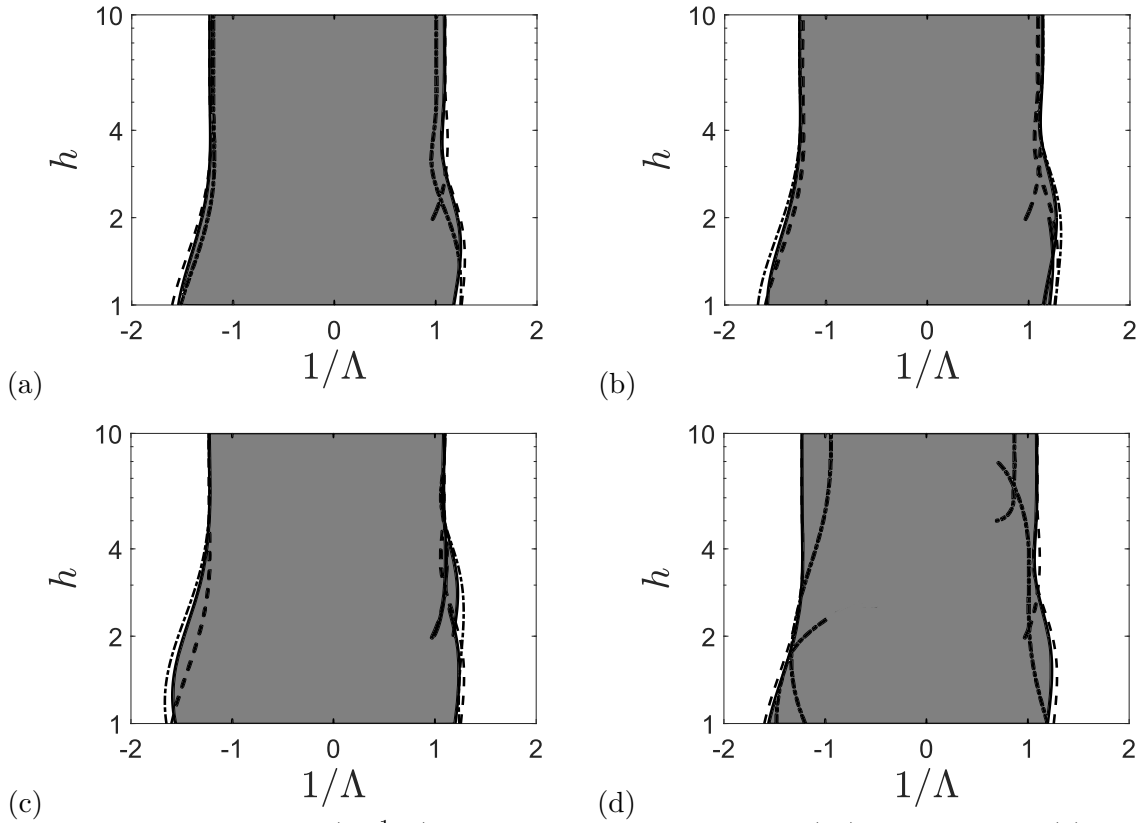

Figure 7: Regions of AI in $(\Lambda^{-1}, h)-$space for the parameters in (40) together with (a) $B^- = 1$, (b) $B^- = 4$, (c) $B^- = 15$ and (d) $B^- = 100$ given by the solid lines. The dashed lines represent the regions of AI for the flow with the symmetric wall configuration with $B^\pm = 2$, while the dot-dashed lines give the symmetric wall configuration with (a) $B^\pm = 1$, (b) $B^\pm = 4$, (c) $B^\pm = 15$ and (d) $B^\pm = 100$.

of confinement ($2.5 \leq h \leq 5$) and $\Lambda^{-1} > 0$. These additional regions are a result of the new WI modes shown in figure 4 becoming dominant over the dominant modes in the symmetric case as we vary h. Further increasing $B^- = 100$ in figure 7(d), however, now appears to have stabilized these regions compared to the symmetric limit. However, as in figure 6, we again find that these asymmetric region plots are confined by the two symmetric wall configurations, suggesting that the symmetric case is the most unstable.

We now consider a vertical slice through figure 7(c) along $\Lambda^{-1} = 1$, to highlight the behaviour of the two families of modes. We consider the dominant AI modes along this slice and track how their growth rates, ω_i, vary as we increase h, presented in figure 8. We compare the results in the $\delta \to 0$ limit to those at different $\delta > 0$ values, because for $\delta > 0$ we can confirm what the correct instability behaviour is, by numerically integrating the Fourier inversion integral (31) and plotting the imaginary part of (34). These results are denoted by the green markers in figure 8. Note, we choose $\delta \neq 0$ but small, as reintroducing the shear layers into the problem introduces a new saddle, labelled S_1 in Juniper (2006), which is capable of dominating the flow at large shear layer thickness values, δ, and large shear values, Λ. At the small δ values we choose, this S_1 saddle remains sub-dominant.

The results show that the value of ω_i^{num} at various δ values agrees with the growth rate curves in figure 8, suggesting that the results in the $\delta \to 0$ limit are correct and robust. We find that increasing the shear layer thickness has the effect of stabilizing the flow, as we would expect of a stabilizing mechanism. What is interesting in this case is that we are able to highlight when AI modes switch dominance at moderate and weak confinements. This confirms what we observe

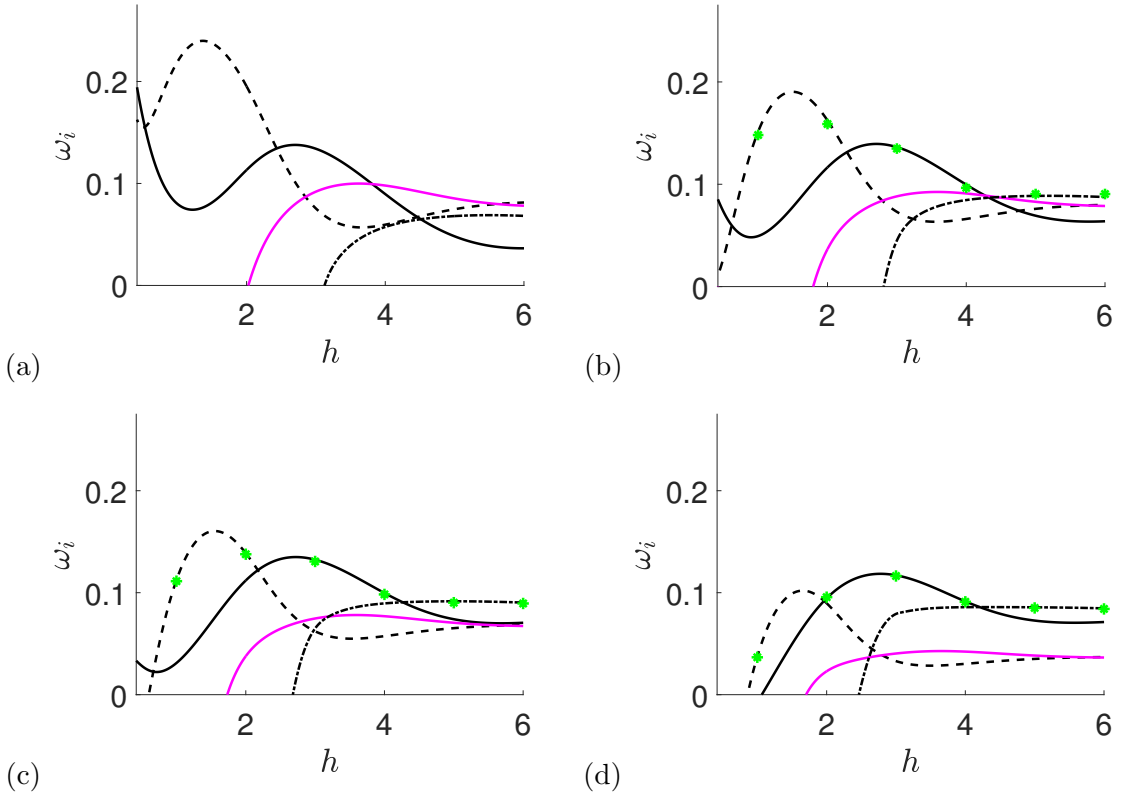

Figure 8: AI growth rates $\omega_i(h)$ with parameters given in figure 7(c), with $\Lambda = 1$ for 4 different δ values: (a) $\delta \to 0$ limit, (b) $\delta = 0.2$, (c) $\delta = 0.3$ and (d) $\delta = 0.5$. The solid black lines represent the original WI_1 mode, while the dashed black line represents the new WI_1' mode represented by the black circle marker in figure 4. The magenta line represents the mode WI_2 and the new WI_2' mode is represented by the dot-dashed line. The green dots indicate the numerical results ω_i^{num} from (34).

in the AI region plot in figure 7(c) at $\Lambda = 1$, i.e. the new modes (modes WI_1, and WI_1') that correspond to the modified wall are distinct and can contribute to the AI response.

4.2 Identical Compliant Walls with Asymmetric Confinement

In this section, we consider both walls to have identical parameters, but we fix $\widetilde{h}$ and vary h to asymmetrically confine the flow. As in the previous section, we first consider the effects of asymmetric confinement on the perturbation velocity eigenmodes for real α and complex ω values by solving equation (27) with $Q^+ = Q^-$. We then consider how the flow's AI characteristics behave at different confinement values.

4.2.1 Velocity Eigenmodes

As in §4.1.1, we will consider the most temporally unstable SI and WI modes and compare the two at different asymmetric confinement configurations. We let $(B, T, K, m, d) = (1, 2, 2, 1.2, 0.001)$, $\Lambda = -2, \widetilde{h} = 2, \alpha = 1$ and we vary h, where $\widetilde{h}$ and h represent the relative non-dimensional positions of the lower and upper walls from the edge of their respective shear layers.. Here we have dropped the $\pm$ notation on the wall parameters with the understanding that these are equal. The eigenmodes are again normalised such that the 2-norm of each mode is equal to one. The vertical perturbation velocity eigenmodes are nearly identical to (35)-(37), except $\Pi^- = \Pi^+ = \Pi$ and the last exponential term in $\widehat{w}^{(5)}(z)$ is now $\Pi \exp(-\alpha(z + 1 + 2\widetilde{h}))$.

Plots of the eigenmodes are presented in figure 9. We find that asymmetric confinement can significantly alter the shapes of these eigenmodes when compared to the symmetric configuration in figures 9(c) and (d). When we strongly confine the flow on one side by setting $h = 1.5$ in figures 9(a) and (b), we find that the unstable WI mode becomes more concentrated at the closer of the two walls. This is particularly apparent when we increase h well beyond the symmetric case in figures 9(e) and (f). In this case $|\widehat{w}| \to 0$ as $z \to 1 + h$ which is the correct behaviour in the unbounded case, while now the WI mode is concentrated at the lower wall. In all cases the shape of the SI modes around the shear layers are largely unaffected by the position of the walls. This suggests that the AI properties of the flow are likely to be dominated by the position of the closest wall.

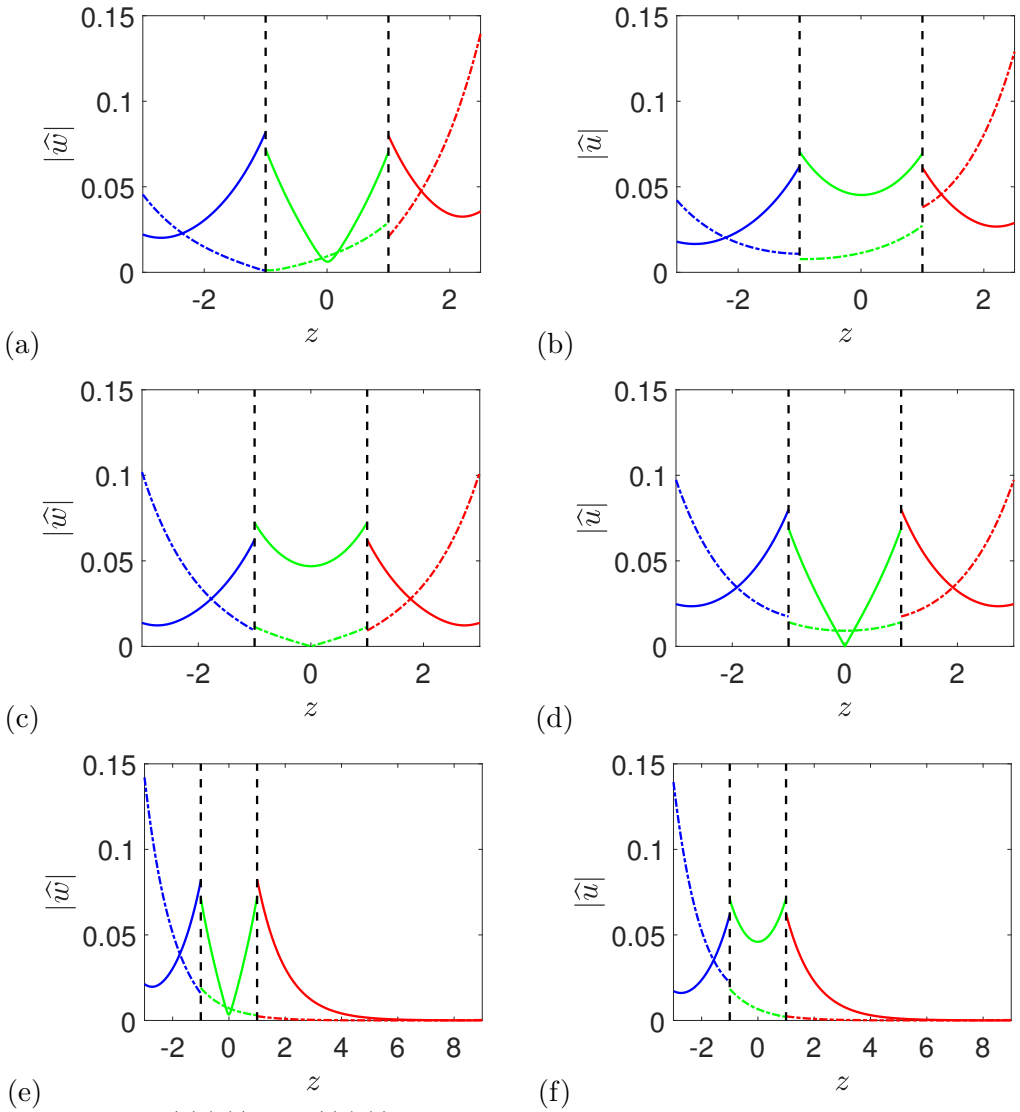

Figure 9: Plots of $|\widehat{w}(z)|$ and $|\widehat{u}(z)|$ at various levels of asymmetric confinement for the most unstable WI mode (dot-dash lines) and the most unstable SI mode (solid lines). We fix $\Lambda = -2, \alpha = 1$ and we fix the lower wall to sit at $z_s^- = -(1+\widetilde{h})$ with $\widetilde{h} = 2$, and the other at $z_s^+ = 1+h$ with (a,b) $h = 1.5$, (c,d) $h = \widetilde{h}$ and (e,f) $h = 8$. Black dashed lines at $z = \pm 1$ indicate the fluid interfaces. These eigenmodes have been normalised such that $||\widehat{w}||_2 = ||\widehat{u}||_2 = 1$.

4.2.2 AI analysis

In this section, we consider the effects of asymmetric confinement of identical compliant walls on the AI characteristics of jets and wakes, and we compare these results to those where the walls symmetrically confine the flow. First we investigate how asymmetric confinement affects the complex α-plane in figure 10 when we have identical compliant confining walls with wall parameters given in (40), and $\Lambda = 1$ and $\widetilde{h} = 2$.

As we move away from the symmetric configuration, given in figure 10(b), we observe that more saddle points appear close to the imaginary α-axis. For other wall configurations, such as the rigid wall limit, these modes can become dominant, however it appears that for our current wall configuration this does not occur, perhaps as a result of the fixed wall being a compliant wall, and thus generating WI modes which tend to be significant generators of AI. We find that the three main modes, the SI mode (blue cross), the WI_1 mode (black cross) and the WI_2 mode (magenta cross) in figure 10, do not move significantly in the α-plane for $h > \widetilde{h}$ in panels (c) and (d), although there is some realignment of the position of the branch points. However, there is more of a movement of these saddles when $h < \widetilde{h}$ in panel (a). This suggests that the stability characteristics of the flow are likely to be more influenced by the closer of the two walls.

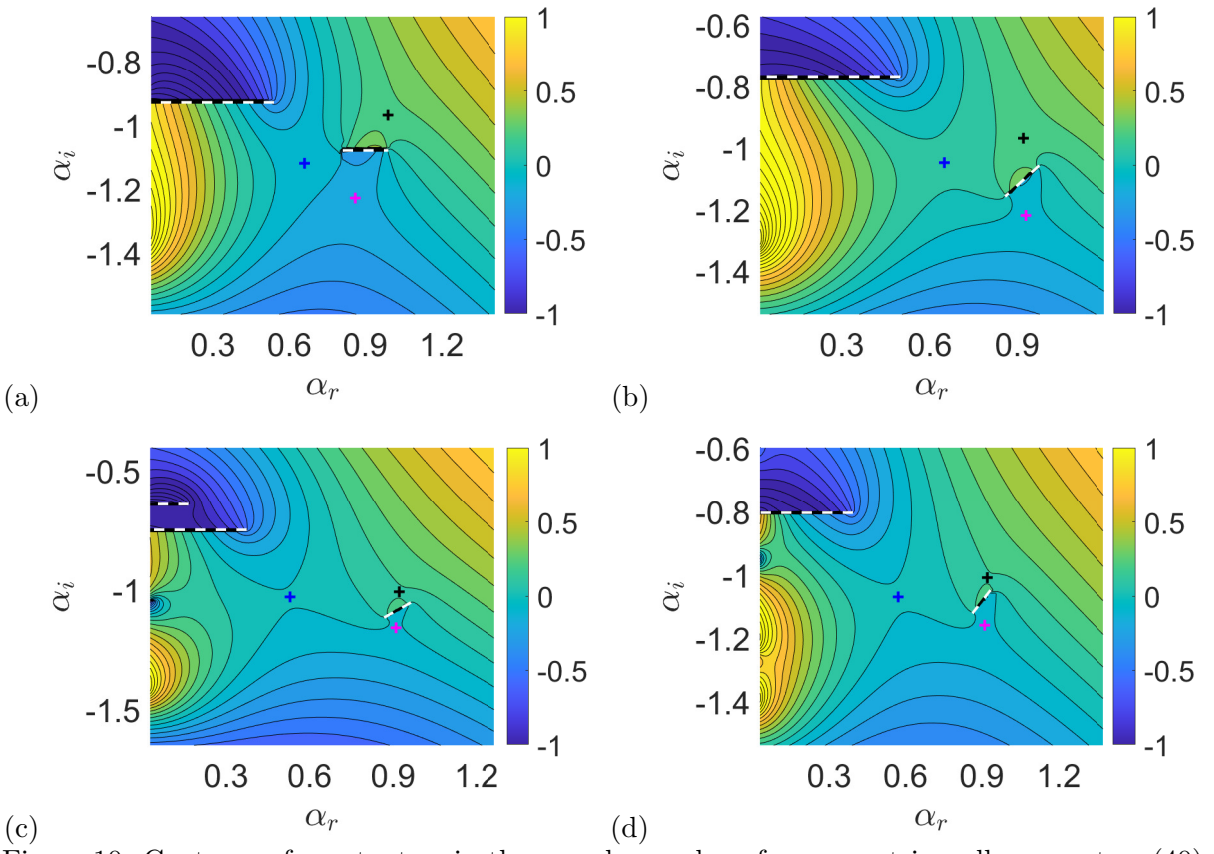

Figure 10: Contours of constant ω_i in the complex α-plane for symmetric wall parameters (40), for $\Lambda = 1, \widetilde{h} = 2$ with (a) $h = 1.5$, (b) $h = \widetilde{h} = 2$, (c) $h = 3$ and (d) $h = 10$. Blue markers indicate SI modes, while black and magenta markers indicate WI modes. Black and white dashed lines represent branch cuts.

We now consider regions of AI in the (Λ^{-1}, h)-plane for three different values of $\widetilde{h}$ in figure 11 along with corresponding figures which specifically plot the locations of the AI region boundaries. The panels compare the AI regions for the symmetrically confined flow with both walls at $z_s^{\pm} = \pm(1 + h)$ (dashed lines) and both walls at $z_s^{\pm} = \pm(1 + \widetilde{h})$ (dot-dashed lines) with the AI regions for the asymmetrically confined flow (solid lines).

In figure 11 the results show that for these parameters the asymmetric AI region is always

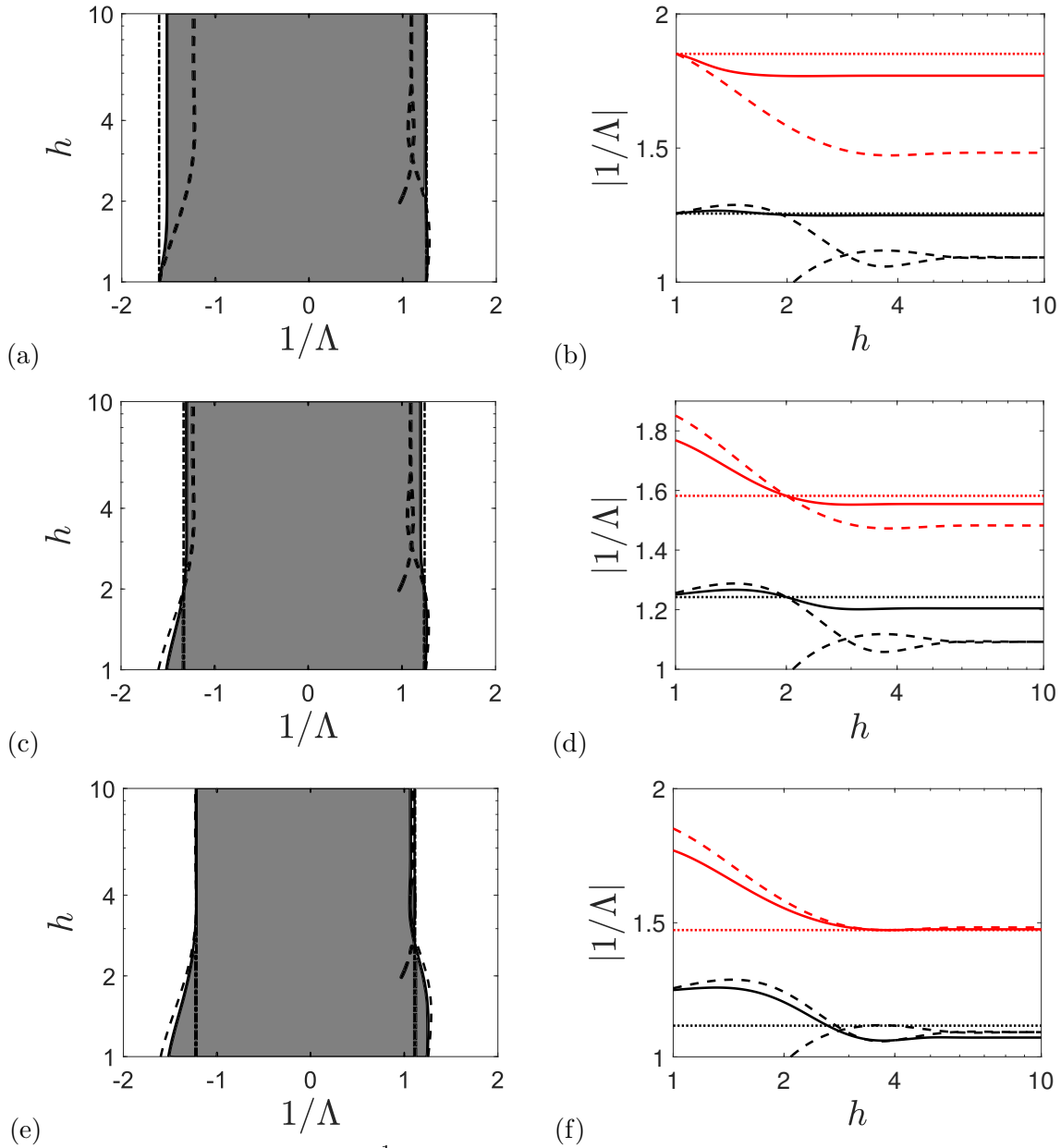

Figure 11: Regions of AI in (Λ^{-1}, h)-space for the parameters in (40) where the fixed wall is placed at $z_s^- = -(1+\widetilde{h})$ with (a,b) $\widetilde{h}=1$, (c,d) $\widetilde{h}=2$, (e,f) $\widetilde{h}=4$ respectively. Panels (a), (c), (e) give the regions of AI in the (Λ^{-1}, h)-plane while (b), (d) and (f) specifically gives the boundaries of these regions. In all cases the solid lines are the asymmetrically confined flow, the dashed lines are the symmetrically confined flow with walls at $z_s^{\pm} = \pm(1+h)$ and the dot-dashed lines are the symmetric flow with walls at $z_s^{\pm} = \pm(1+\widetilde{h})$. In (b), (d), (f) the black lines are for jets ($\Lambda^{-1} > 0$) and red lines are for wakes ($\Lambda^{-1} < 0$) whose values have been shifted up the vertical axis by a constant.

bounded by the two symmetric regions, suggesting that the largest region of AI (i.e. is most absolutely unstable) is the symmetric case. However, there is one interesting feature to draw from these figures, and that is that it is not always the most confined symmetric wall case which leads to the largest region of AI. In figure 11(b) for $1 < h < 2$, $\widetilde{h} = 1$ and $\Lambda^{-1} > 0$ the dashed line gives the largest region of AI, which is the least confining of the two symmetrically confining results. If the most confining symmetric case was always the most unstable case then we would expect the dashed line to give the largest $|\Lambda^{-1}|$ values for $h < \widetilde{h}$ and the dot-dashed line to give

the largest $|\Lambda^{-1}|$ values for $h > \widetilde{h}$.

We now take a vertical slice through the AI region shown in figure 11(c) along $\Lambda^{-1} = 1$, and compare how the growth rates of the dominant pinch points vary with h. Again, we examine the robustness of these results by plotting the numerical growth rates ω_i^{num} from (34) as green markers, shown in figure 12 for $\delta = 0.2$. We find that for these wall parameter values there is

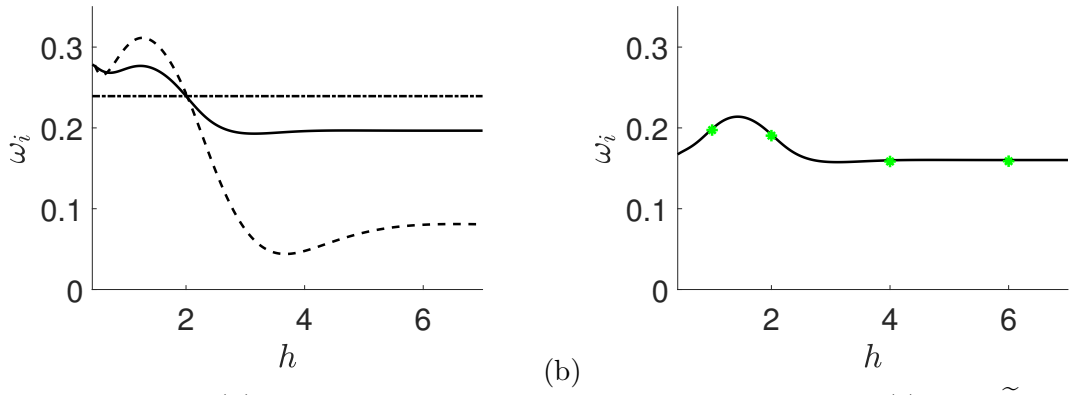

Figure 12: Plot of $\omega_i(h)$ for the most unstable WI mode from figure 11(c) with $\widetilde{h} = 2$ and $\Lambda^{-1} = 1$. Panel (a) denotes the $\delta \to 0$ case and (b) shows the case where $\delta = 0.2$. In (a) the 3 results correspond to the growth rates for the modes seen in 11(c) with the same line styles. The green dots in (b) indicate the numerical results ω_i^{num} from (34).

only a single WI mode which we need to consider to fully calculate the AI properties of the flow. Much like in §4.1 we find that increasing the shear layer thickness results in the stabilization of the WI modes for all h values considered. In panel (a) we also consider the corresponding AI growth rates for the most unstable modes in the symmetrically confined case for $z_s^{\pm} = \pm(1+h)$ (dashed line) and $z_s^{\pm} = \pm(1+\widetilde{h})$ (dot-dashed line). These results show that the most unstable case (largest ω_i) appears to be the strongest confined symmetric result, except for $h \approx 1$, where there is a small region where the asymmetric result is more unstable. These results show that while typically the symmetrically confined flow is most unstable, there are small regions of parameter space where the asymmetrically confined flow is most unstable. However, in this case the strong confinement means this result is likely to be strongly affected by any viscous boundary layers at the walls in a realistic flow setup.

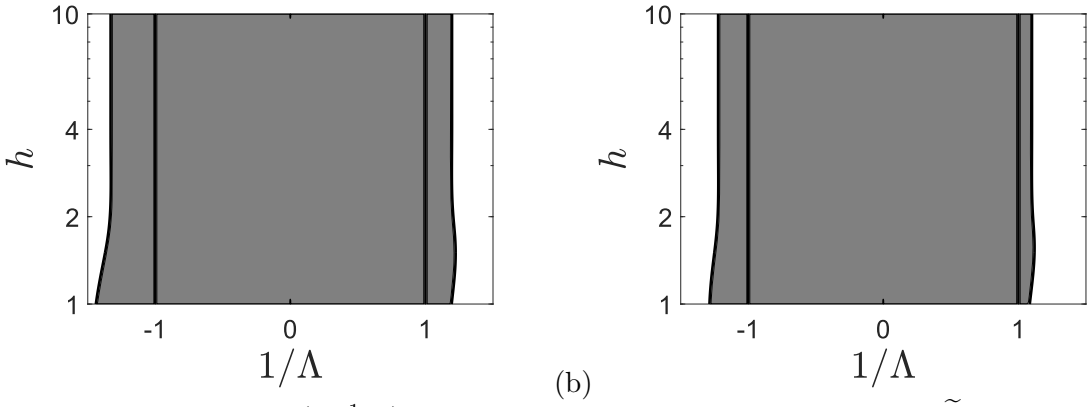

Figure 13: Regions of AI in (Λ^{-1}, h) space for the parameters in figure 11 with $\widetilde{h} = 1.5$ for finite shear layer thickness (a) $\delta = 0.2$, (b) $\delta = 0.5$. The vertical lines give the values of $\Lambda = \pm 1$ which are the contribution from the neglected S_1 saddle for comparison (Rees and Juniper, 2010)

In figure 13 we consider the effect of increasing the shear layer thickness on the regions of AI for the (Λ^{-1}, h)-plane plot in figure 11 with $\widetilde{h} = 1.5$. What we observe is that the regions of AI decrease with increasing δ, which agrees with the observation from the symmetrically confined

flow study in Poole (2024).

4.3 Rigid Walls with Asymmetric Confinement

Finally, in this section we consider the rigid wall limit of (27) and examine how asymmetric confinement affects the AI properties of the jet/wake flow.

4.3.1 Velocity Eigenmodes

In this case there are no WI modes, hence we just have a single SI mode to consider, which is equivalent to a sinuous mode in the symmetric case. The vertical perturbation velocity eigenmodes take a similar form to (35), with $\Pi^{\pm} = 1$ and the last exponential term in $\widehat{w}^{(5)}(z)$ taking the form $\exp(-\alpha(z+1+2\widetilde{h}))$. These eigenmodes are plotted for 3 different confinement configurations in figure 14.

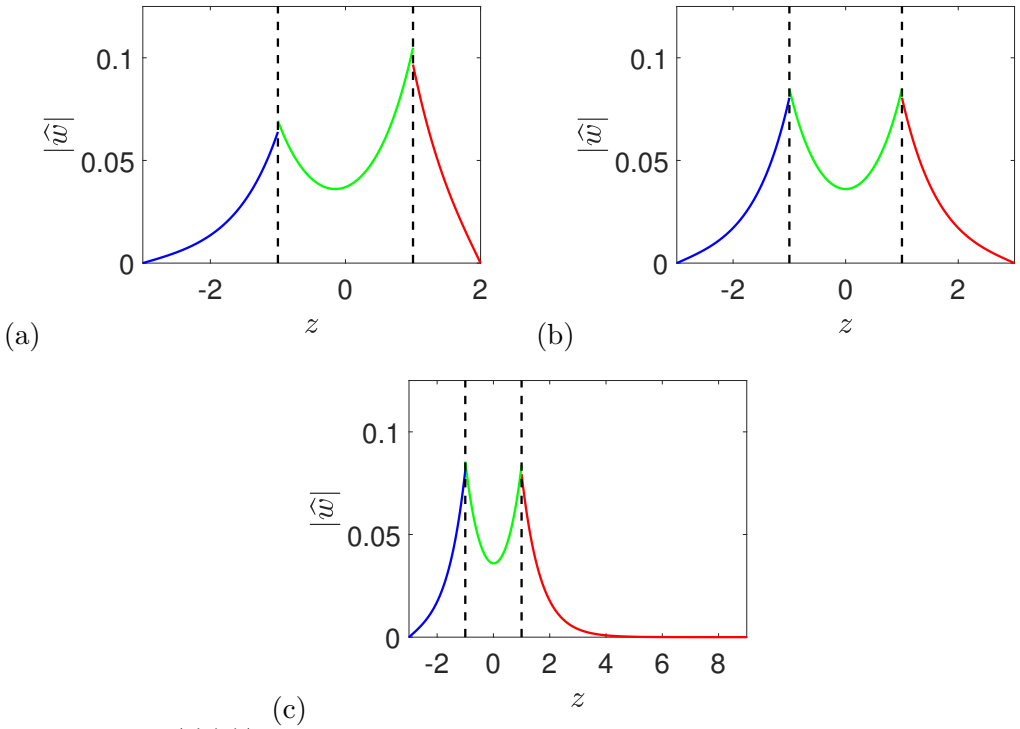

Figure 14: Plots of $|\widehat{w}(z)|$ at various levels of asymmetric confinement for the most unstable SI mode. We fix $\Lambda = -2, \alpha = 1.5$ and we fix one wall to sit at $z_s^- = -(1+\widetilde{h})$ with $\widetilde{h} = 2$ and the other at $z_s^+ = 1+h$ with (a) $h = 1$, (b) $h = \widetilde{h}$ and (c) $h = 8$. Black dashed lines at $z = \pm 1$ indicate the fluid interfaces. The eigenmodes are normalised such that $||\widehat{w}||_2 = 1$.

What we observe is that the shape of the modes are not hugely affected by the level of confinement, which agrees with what was seen for the SI modes when the walls were compliant surfaces. It is not until we strongly confine the flow with $\widetilde{h} = 1$ in figure 14(a) that we see a discernible difference in the shape. However, despite this seeming similarity to the results in §4.1 and §4.2, we find that without the presence of the WI modes there appears to be more mode interactions between SI modes and so we need to consider the effect of this.

4.3.2 AI analysis

In this section, we consider the effect of asymmetric confinement of rigid walls on the AI characteristics of the flow. We again fix $\widetilde{h}$ and let h vary. In figure 15 we consider how the α-plane varies with h. We observe that modes which were dominant in the symmetric limit (denoted here

with a red cross) are able to switch dominance with new modes (represented by the red circle) as a result of the the asymmetric confinement of the flow. For the parameters in this figure the new mode (red circle) emerges from the vicinity of the imaginary α-axis and as h increases, the original mode (red cross) moves off towards this axis. For the parameters considered, the saddle in panel (d) has a smaller value of ω_i to that in panel (a) which suggests that the flow which is closer to being symmetrically confined appears to be more absolutely unstable.

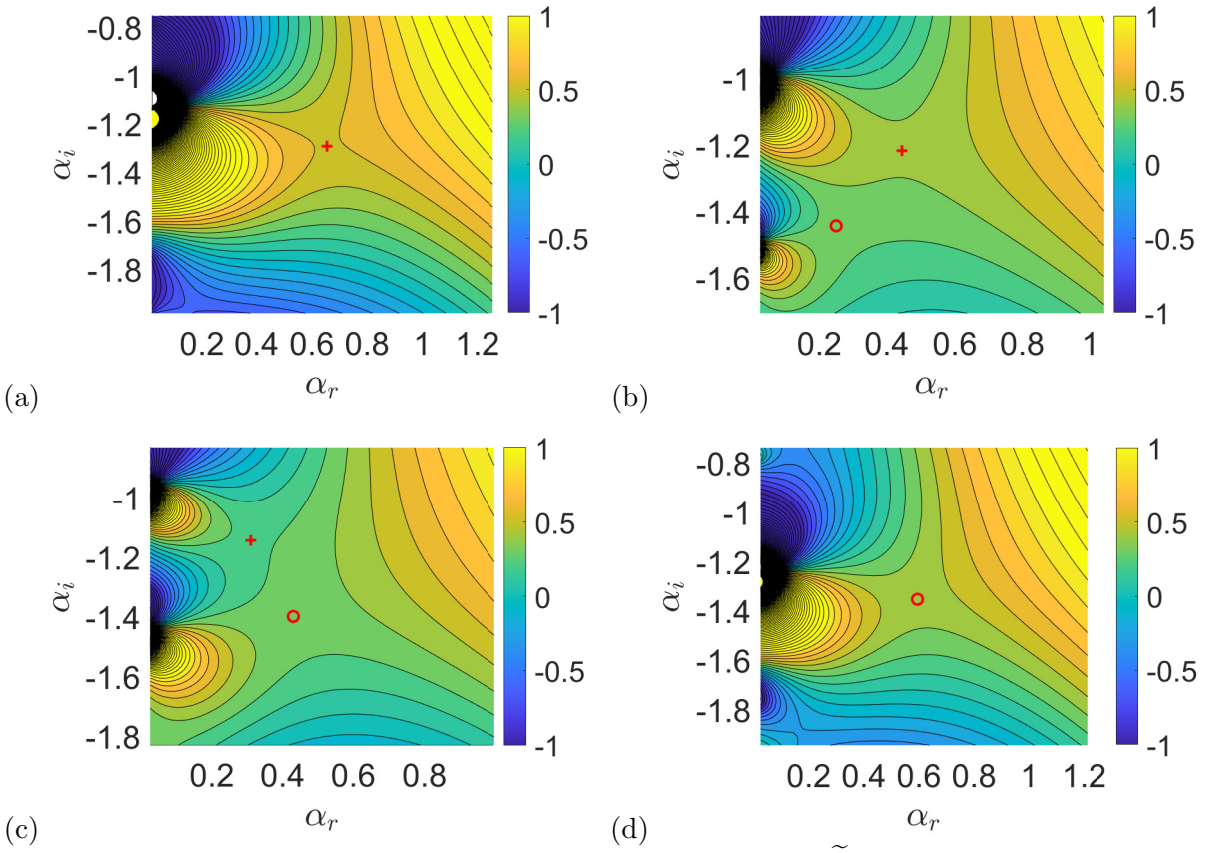

Figure 15: Contours of constant ω_i in the complex $\alpha-$plane for $\widetilde{h} = 1.5, \Lambda = 1.67$, as we vary (a) $h = 2$, (b) $h = 2.7$, (c) $h = 2.9$ and (d) $h = 4$. The red cross and circle identify two pinch points which dominate the AI characteristics of the flow in panels (a) and (d) respectively.

In figure 16 we compare the regions of AI in (Λ^{-1}, h)-parameter space as well as the bounding values of $|\Lambda^{-1}|$ for the asymmetric case (solid lines) and the symmetric confined flows with $z_s^{\pm} = \pm(1+h)$ (dashed lines) and $z_s^{\pm} = \pm(1+\widetilde{h})$ (dot-dashed lines). When there are no WI modes present the boundaries of the AI regions become more complex, but as in §4.2 we find that the AI region is largest in one of the two corresponding symmetrically confined scenarios, i.e. the symmetric case appears again to be the most absolutely unstable. This observation is backed up by figure 17 which shows the growth rates for a wake flow from figure 15 with $\widetilde{h} = 1.5$ and $\Lambda^{-1} = -1$. Here we see that the asymmetric result always has a smaller growth rate than the strongest confined symmetric case. Thus it again appears that the symmetrically confined results are most absolutely unstable in line with the findings of Wang et al. (2019) for the temporal stability of wakes.

5 Conclusions

We considered the asymmetric confinement of homogeneous jet/wake flows by compliant walls. In particular we considered two approaches to generating asymmetry, symmetrically confining

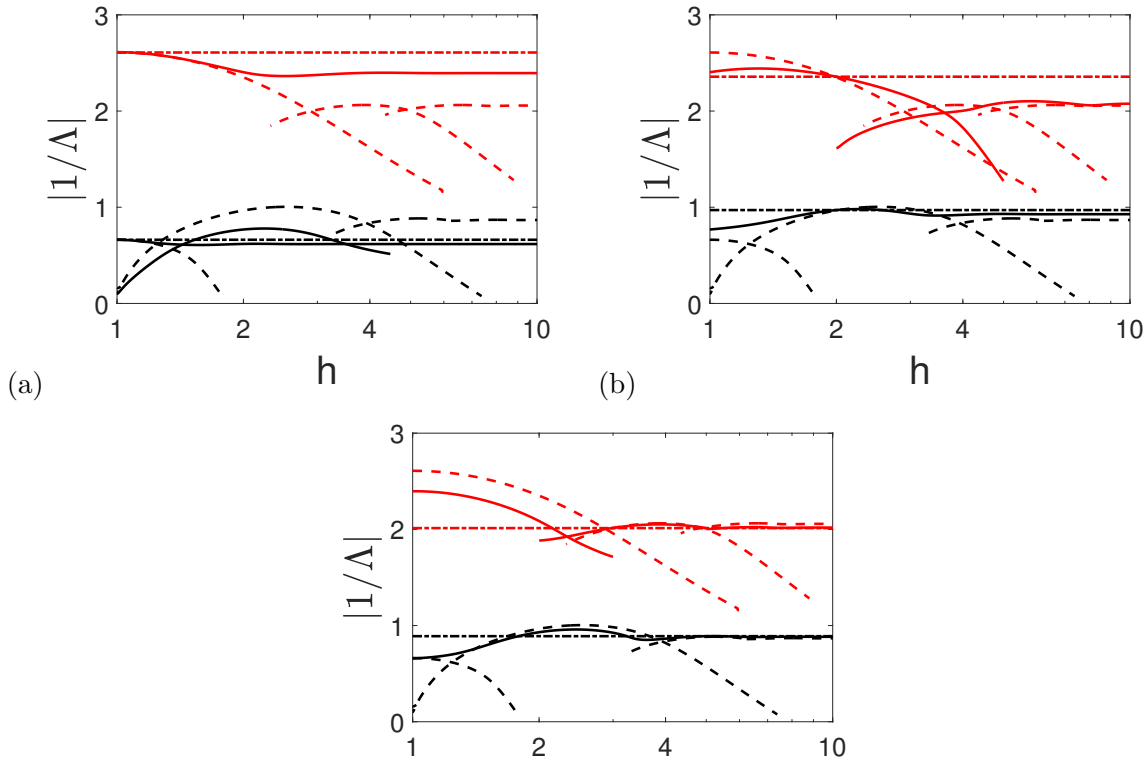

Figure 16: The AI-CI boundaries of the AI regions in (Λ^{-1}, h)-space for rigid walls where the fixed wall is placed at $z_s^- = -(1+\widetilde{h})$ with (a) $\widetilde{h} = 1$, (b) $\widetilde{h} = 2$, (e) $\widetilde{h} = 5$ respectively. Solid lines denote the asymmetrically confined flow, the dashed lines denote the symmetrically confined flow with walls at $z_s^{\pm} = \pm(1+h)$ and the dot-dashed lines denote the symmetric flow with walls at $z_s^{\pm} = \pm(1+\widetilde{h})$. The black lines are for jets ($\Lambda^{-1} > 0$) and red lines are for wakes ($\Lambda^{-1} < 0$) whose values have been shifted up the vertical axis by a constant.

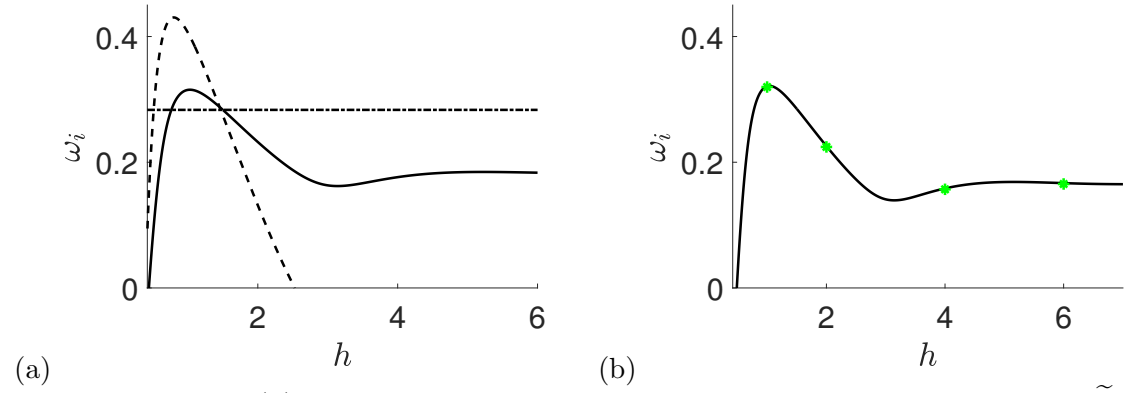

Figure 17: Plot of $\omega_i(h)$ for the dominant saddle for a wake mode from figure 16 with $\widetilde{h} = 1.5$, with $\Lambda^{-1} = -1$ and (a) the $\delta \to 0$ limit (solid line) and (b) $\delta = 0.2$. In (a) the dashed line indicates the symmetric confinement configuration, with both walls at $z = \pm(1+h)$, while the dash-dotted line indicates the growth rate in the symmetric limit, and (b) $\delta = 0.2$. The green dots indicate the numerical results ω_i^{num} from (34).

the flow with non-identical compliant walls, and asymmetrically confining the flow with identical compliant walls. In the first case we found that varying the wall parameters of one wall introduced a new family of AI modes. The results presented suggest that when the walls are of different construction, but symmetrically confining, then it is the lighter, more flexible (least

rigid) wall which dictates the overarching AI characteristics of the flow.

In the second case we found that in most scenarios the AI characteristics of the flow were driven by the wall-induced modes of the most confining wall. However, when the size of the AI region in parameter space, and some typical growth rates, were compared to the symmetrically confined flow, where both walls were at their closest to the shear layers, we found that this symmetric flow was more absolutely unstable than the asymmetric flow. This observation was also seen for the case of two rigid walls asymmetrically confining the flow.

This study therefore suggests that the symmetrically confined flow setup is generally the most absolutely unstable set up, even when compliant walls are considered. However, the possibility was observed in figure 11 that the size of parameter space for asymmetric compliant walls could be larger than the symmetric case at small h values. In this work we downplayed this finding as the confining parameter $h < 1.5$, a threshold value below which viscous effects can have a significant stabilizing effect on 'more realistic' flows than our inviscid flow assumption (Tammisola et al., 2011). However, the fact that we have not explored a large region of the flow and wall parameter space, which is $\mathbb{R}^8$, means that there could be a more optimal wall configuration that allows this destabilization to occur at weaker confinement values, with more details discussed in Poole (2024). It might also be possible to identify other flows where compliant walls can increase the flow's ability to sustain an AI, and one possibility is the mixing layer flow, as Healey (2009) showed that asymmetric confinement by rigid walls in this case can cause the flow to be more absolutely unstable. A simpler scenario such as this single mixing layer may also be more conducive to examining a larger amount of the above parameter space.

6 Acknowledgements

RP would like to thank the EPSRC for funding his PhD studentship under grant EP/V520111/1 and MRT is supported by the EPSRC under grant number EP/W006545/1. For the purpose of open access, the authors have applied a Creative Commons Attribution (CC BY) licence to any Author Accepted Manuscript version arising.

References

Brambley, E. J. (2009). Fundamental problems with the model of uniform flow over acoustic linings. J. Sound Vib., **322**(4-5), 1026–1037.

Briggs, R. J. et al. (1964). Electron-stream interaction with plasmas, volume 187. MIT press Cambridge, MA.

Drazin, P. G. (2002). Introduction to hydrodynamic stability, volume 32. Cambridge University Press.

Drazin, P. G. and Reid, W. H. (2004). Hydrodynamic stability. Cambridge university press.

Emerson, B., Jagtap, S., Quinlan, J. M., Renfro, M. W., Cetegen, B. M., and Lieuwen, T. (2016). Spatio-temporal linear stability analysis of stratified planar wakes: Velocity and density asymmetry effects. Phys. Fluids, **28**(4), 045101.

Healey, J. J. (2006). A new type of convective instability with exponential growth perpendicular to the basic flow. J. Fluid Mech., **560**, 279–310.

Healey, J. J. (2007). Enhancing the absolute instability of a boundary layer by adding a far-away plate. J. Fluid Mech., **579**, 29.

Healey, J. J. (2009). Destabilizing effects of confinement on homogeneous mixing layers. J. Fluid Mech., **623**, 241–271.

Huerre, P. and Monkewitz, P. A. (1990). Local and global instabilities in spatially developing flows. Annu. Rev. Fluid Mech., **22**(1), 473–537.

Juniper, M. P. (2006). The effect of confinement on the stability of two-dimensional shear flows. J. Fluid Mech., **565**, 171.

Juniper, M. P. (2007). The full impulse response of two-dimensional jet/wake flows and implications for confinement. J. Fluid Mech., **590**, 163.

Juniper, M. P. and Candel, S. M. (2003). The stability of ducted compound flows and consequences for the geometry of coaxial injectors. J. Fluid Mech., **482**, 257–269.

Juniper, M. P., Tammisola, O., and Lundell, F. (2011). The local and global stability of confined planar wakes at intermediate reynolds number. J. Fluid Mech., **686**, 218–238.

Poole, R. (2024). The Effects of Wall Compliance on the Stability of Jets and Wakes. Ph.D. Thesis, University of Surrey.

Poole, R. and Turner, M. R. (2023). Stability of jets and wakes confined by compliant walls. Phys. Rev. Fluids, **8**(6), 063901.

Rees, S. and Juniper, M. (2010). The effect of confinement on the stability of viscous planar jets and wakes. J. Fluid Mech., **656**, 309.

Rienstra, S. W. and Darau, M. (2011). Boundary-layer thickness effects of the hydrodynamic instability along an impedance wall. J. Fluid Mech., **671**, 559–573.

Schmid, P. J., Henningson, D. S., and Jankowski, D. F. (2002). Stability and transition in shear flows. applied mathematical sciences, vol. 142. Appl. Mech. Rev., **55**(3), B57–B59.

Smith, D. M. (1991). Algorithm 693: A fortran package for floating-point multiple-precision arithmetic. ACM Trans. Math. Softw., **17**(2), 273–283.

Tammisola, O., Lundell, F., Schlatter, P., Wehrfritz, A., and Söderberg, L. D. (2011). Global linear and nonlinear stability of viscous confined plane wakes with co-flow. J. Fluid Mech., **675**, 397–434.

Wang, S., Wen, F., Shi, X., and Zhou, X. (2019). Stability analysis of asymmetric wakes. Phys. Fluids, **31**(6), 064108.

Weilgart, L. (2018). The impact of ocean noise pollution on fish and invertebrates. Report for OceanCare, Switzerland.